iScience

CellPress

Article

Low-Energy-Loss Polymer Solar Cells with 14.52% Efficiency Enabled by Wide-Band-Gap Copolymers

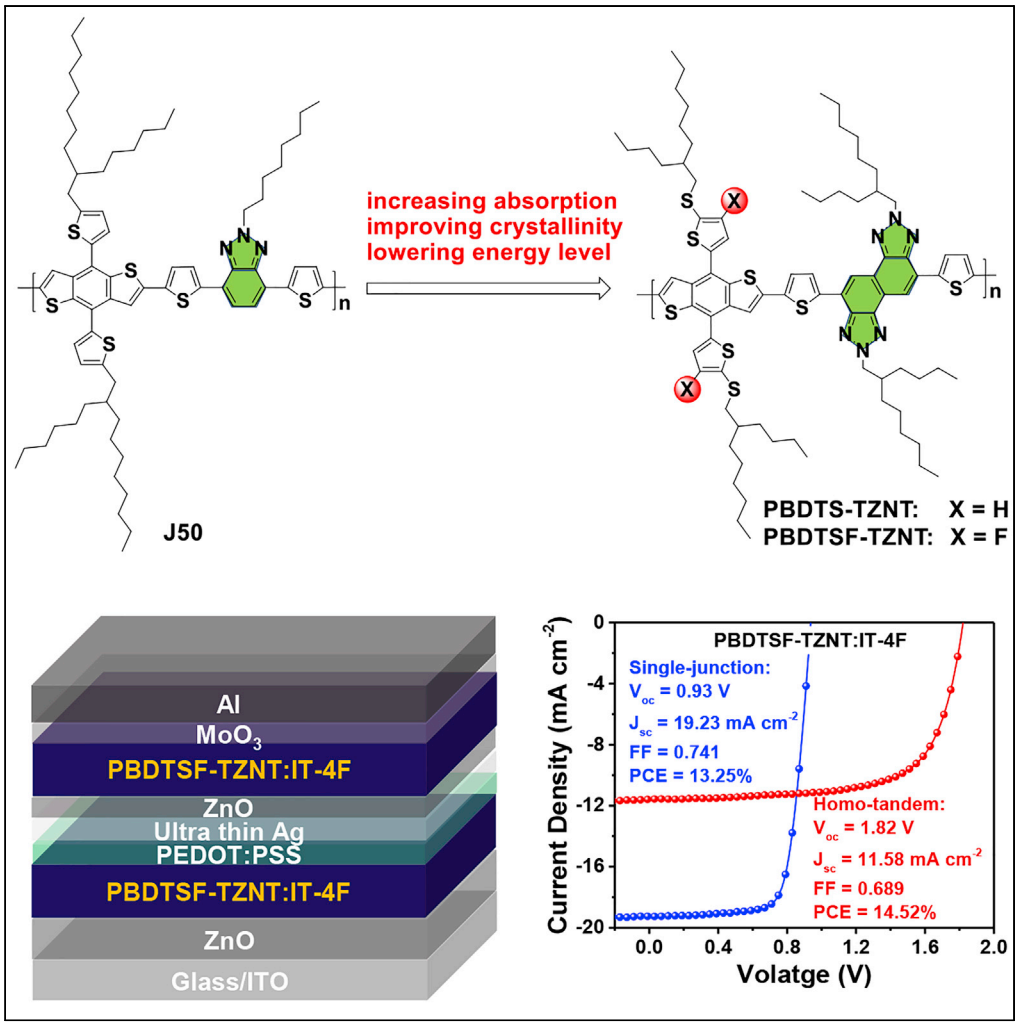

Kui Feng, Jian Yuan, Zhaozhao Bi, Wei Ma, Xiaopeng Xu, Guangjun Zhang, Qiang Peng

msewma@mail.xjtu.edu.cn (W.M.)
qiangpengjohnny@yahoo.com (Q.P.)

HIGHLIGHTS

High-performance TZNT-based wide-band-gap copolymers were designed and synthesized

The rigid planar backbone induced high crystallinity and good molecular packing

Sulfuration and fluorination fine-tuned HOMO aiming for high V_{oc} and low E_{loss}

Single-junction and homo-tandem devices exhibited high PCEs of 13.25% and 14.52%

Feng et al., iScience *12*, 1–12
February 22, 2019
https://doi.org/10.1016/j.isci.2018.12.027

iScience

CellPress

Article

Low-Energy-Loss Polymer Solar Cells with 14.52% Efficiency Enabled by Wide-Band-Gap Copolymers

Kui Feng,[1] Jian Yuan,[2] Zhaozhao Bi,[2] Wei Ma,[2,*] Xiaopeng Xu,[1] Guangjun Zhang,[1] and Qiang Peng[1,3,*]

SUMMARY

Two wide band-gap copolymers poly[4,8-bis(5-(2-butylhexylthio)thiophen-2-yl)benzo[1,2-b:4,5-b′]dithiophene-2,6-diyl-*alt*-TZNT] (PBDTS-TZNT) and poly[4,8-bis(4-fluoro-5-(2-butylhexylthio)thiophen-2-yl)benzo[1,2-b:4,5-b′]dithiophene-2,6-diyl-*alt*-TZNT] (PBDTSF-TZNT) based on naphtho[1,2-c:5,6-c]bis(2-octyl-[1,2,3]triazole) (TZNT) and benzo[1,2-b:4,5-b′]dithiophene (BDT) with different conjugated side chains have been developed for efficient nonfullerene polymer solar cells (NF-PSCs). The rigid planar backbone of BDT and TZNT units imparted high crystallinity and good molecular stacking property to these copolymers. Using 3,9-bis(2-methylene-(3-(1,1-dicyanomethylene)-indanone)-5,5,11,11-tetrakis(4-hexylphenyl)-dithieno[2,3-d:2′,3′-d′]-s-indaceno[1,2-b:5,6-b′]-dithiophene (ITIC) as the acceptor, PBDTSF-TZNT devices showed a high V_{oc} of 0.98 V with an E_{loss} of 0.61 eV. On selecting 3,9-bis(2-methylene-(5,6-difluoro-(3-(1,1-dicyanomethylene)-indanone)-5,5,11,11-tetrakis(4-hexylphenyl)-dithieno[2,3-d:2′,3′-d′]-s-indaceno[1,2-b:5,6-b′]-dithiophene (IT-4F) instead of ITIC, the devices maintained the high V_{oc} of 0.93 V with an even lower E_{loss} of 0.59 eV. The combination of the above-mentioned low E_{loss}, broadened absorption, better matched energy level, improved crystallinity, and fine-tuned morphology promoted the power conversion efficiency (PCE) of PBDTSF-TZNT:IT-4F devices from 12.16% to 13.25%. Homo-tandem devices based on PBDTSF-TZNT:IT-4F subcells further enhanced the light-harvesting ability and boosted the PCE of 14.52%, which is the best value for homo-tandem NF-PSCs at present.

INTRODUCTION

Polymer solar cells (PSCs), which contain a nanophase-separated bicontinuous network of a *p*-type conjugated polymer donor and an *n*-type semiconductor acceptor, have received considerable attention owing to their unique prospects for achieving low cost, light weight, and mechanical flexibility in solar energy applications (Cheng et al., 2009; Li et al., 2012; Zhang et al., 2018b). During the past few years, nonfullerene acceptors (NFAs) have aroused intense interest because of the synthetic flexibility and great potential to overcome the intrinsic drawbacks of the fullerene counterparts (Lin and Zhan, 2016; Yan et al., 2018; Zhang et al., 2018b). Particularly, planar acceptor-donor-acceptor (A-D-A)-type NFAs presented low band gaps (LBGs) with good absorptions, readily tunable energy levels, and superior photovoltaic performance (Cui et al., 2017; Li et al., 2016; Lin et al., 2015a, 2015b, 2016; Lin and Zhan, 2016; Xu et al., 2017; Yan et al., 2018; Zhang et al., 2018b). State-of-the-art power conversion efficiencies (PCEs) exceeding 13% for single-junction nonfullerene PSCs (NF-PSCs) (Li et al., 2018a; Xiao et al., 2017; Zhang et al., 2018c, 2018d; Zheng et al., 2018) and 17% for tandem NF-PSCs (Meng et al., 2018) have been realized, showing a bright future for practical applications.

To make full use of the present excellent LBG NFAs, developing high-performance wide-band-gap (WBG) donor copolymers has become a hot research topic (Cai et al., 2017). WBG copolymers have strong absorption in the short wavelength region, which can match well with LBG NFAs to realize a complementary absorption and then an improved photocurrent in NF-PSCs (Xu et al., 2018a, 2018b). Besides the issue of complementary absorption, low-lying highest occupied molecular orbital (HOMO) level and appropriate molecular aggregation of the WBG donor are equally important for achieving high PCE because the HOMO level and molecular packing can directly influence the open-circuit voltage (V_{oc}) and charge carrier mobility (Cai et al., 2017; Li et al., 2018a; Xu et al., 2018b). Among the efficient material systems of WBG copolymers, benzotriazole (BTA)-based donor-acceptor copolymers have received wide research interests. Such types of copolymers provide an advantage of incorporating soluble alkyl chains onto the BTA skeleton rather than on the thiophene bridges of other WBG copolymers, which can also reduce the steric repulsion between the adjacent segments for more planar π-conjugations (Min et al., 2011; Price et al., 2011). Therefore,

[1]Key Laboratory of Green Chemistry and Technology of Ministry of Education, College of Chemistry, State Key Laboratory of Polymer Materials Engineering, Sichuan University, Chengdu 610064, PRC

[2]State Key Laboratory for Mechanical Behavior of Materials, Xi'an Jiaotong University, Xi'an 710049, PRC

[3]Lead Contact

*Correspondence: msewma@mail.xjtu.edu.cn (W.M.), qiangpengjohnny@yahoo.com (Q.P.)

https://doi.org/10.1016/j.isci.2018.12.027

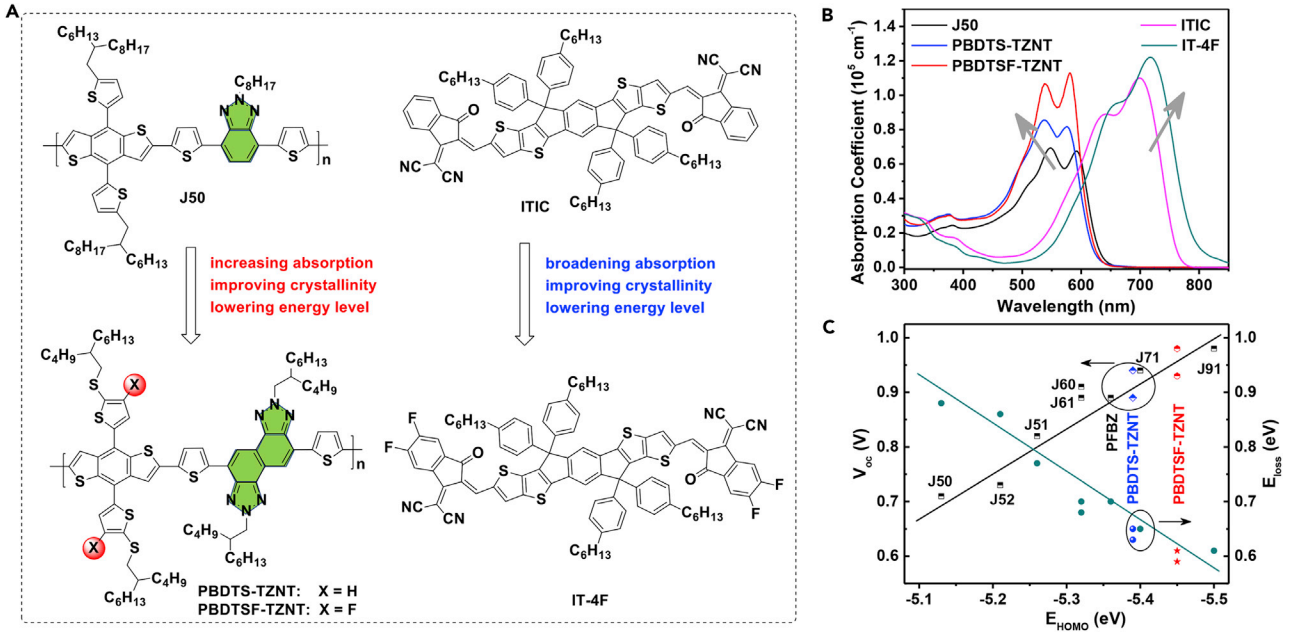

Figure 1. Design of Wide-Band-Gap Copolymer Donors with Low-Lying HOMO Level

(A) Molecular structures of the copolymers and NFAs.

(B) Absorption profiles of the copolymers and NFAs.

(C) Summarized V_{oc} and E_{loss} versus E_{HOMO}.

BTA-based copolymers exhibited excellent solubility, strong absorption, and high charge carrier mobility. Extensive studies combining side chain engineering and fluorination strategies have been made (Bin et al., 2016a, 2016b; Min et al., 2012; Price et al., 2011; Xue et al., 2017), and have increased the PCE to over 12% (Lin et al., 2018; Liu et al., 2018; Luo et al., 2018; Zhao et al., 2017a, 2018). With respect to the above-mentioned molecular design, extending the π-conjugation of the building blocks has been proved to be positive for more ordered molecular packing, improved intramolecular charge transfer transition, enhanced absorption, and thus elevated photovoltaic performance (Dong et al., 2013; Osaka and Takimiya, 2017; Wang et al., 2011; Yu et al., 2017). Based on this, naphtho[1,2-c:5,6-c]bis(2-octyl-[1,2,3]triazole) (TZNT) was developed to construct high-performance donor copolymers, which fused two BTA units with an angular shape (Dong et al., 2013). Apart from the advantages discussed above, the enhanced electron deficit of TZNT could also lower the HOMO level of the resulting copolymers, contributing to high V_{oc}s and PCEs in fullerene PSCs (Dong et al., 2013; Lan et al., 2015). Apart from the above two reports, most recently, a high PCE of over 10% for a new TZNT-based copolymer of PDTF-TZNT has been first realized in NF-PSCs by our group (Tang et al., 2018b). However, the relatively high HOMO level (−5.24 eV) caused by the strong electron-donating donor block of thiophene led to low V_{oc} (0.8 V) and large energy loss (E_{loss} = 0.8 eV, defined as $E_{loss} = E_g^{opt} - qV_{oc}$, where E_g^{opt} is the optical band gap and q is the elementary charge). To further increase the V_{oc} and reduce the E_{loss}, the electron-donating strength of the incorporated donor blocks should be weakened.

In terms of light harvesting, it is still a great challenge for achieving panchromatic absorption by just using a single active layer due to the limited absorption ability. A successful and universal strategy to elevate the device performance is to use tandem configurations. Tandem solar cells connect multiple photoactive layers by highly transparent interconnecting layers (Shim et al., 2012; Vasilopoulou et al., 2015), offering more efficient light-harvesting ability than single-junction solar cells due to enhanced light trapping without sacrificing charge transport property, which can induce high V_{oc} and PCE (Li et al., 2013; Zuo et al., 2014).

Herein, we report the design and synthesis of two novel WBG copolymers, poly[4,8-bis(5-(2-butylhexylthio) thiophen-2-yl)benzo[1,2-b:4,5-b′]dithiophene-2,6-diyl-*alt*-TZNT] (PBDTS-TZNT) and poly[4,8-bis(4-fluoro-5-(2-butylhexylthio)thiophen-2-yl)benzo[1,2-b:4,5-b′]dithiophene-2,6-diyl-*alt*-TZNT] (PBDTSF-TZNT), based on TZNT and benzo[1,2-b:4,5-b′]dithiophene (BDT) blocks for realizing highly efficient NF-PSCs (Figure 1 and Scheme 1). BDT unit, a promising weak electron-donating donor block, possesses a rigid and

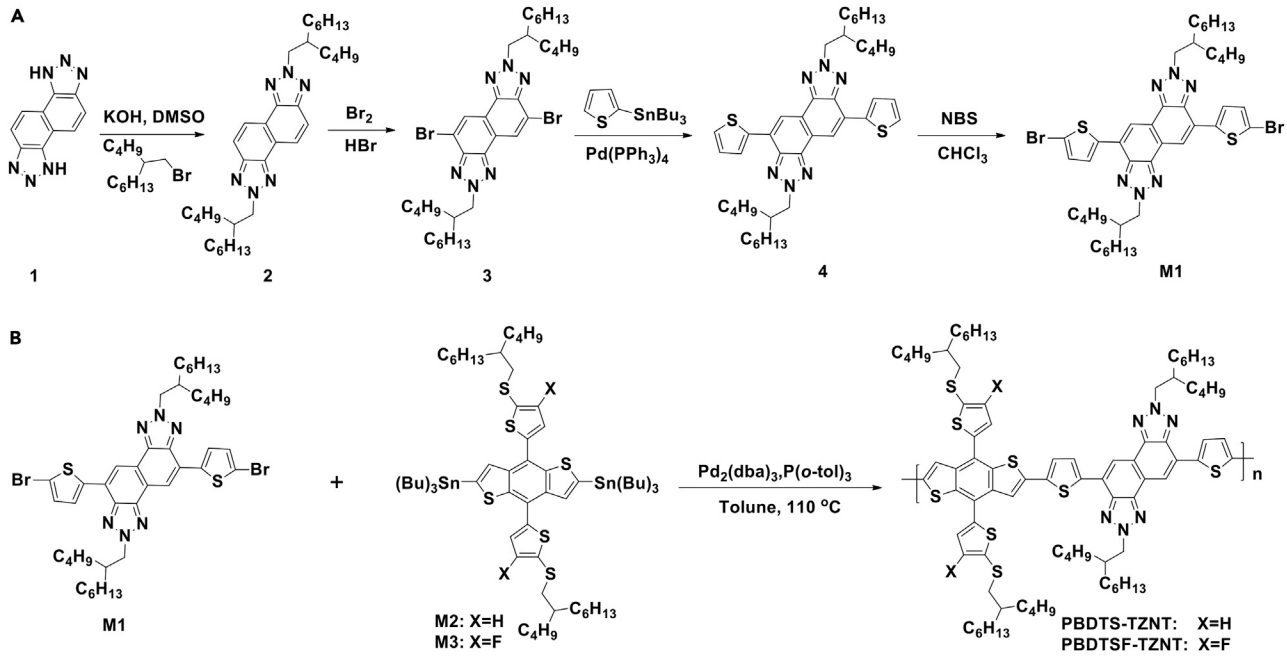

Scheme 1. Synthetic Routes of the Monomers and Copolymers

(A) Synthetic route of monomer M1.

(B) Synthetic routes of PBDTS-TZNT and PBDTSF-TZNT.

Also see Figure S1.

large coplanar structure for inducing a strong π-π stacking (Ye et al., 2014). Energy level, absorption spectrum, crystallinity, charge carrier mobility, and blend morphology can be feasibly tailored by manipulating the two-dimensional (2D) conjugated side chains of BDT (Bin et al., 2016a, 2016b; Fan et al., 2017, 2018; Fei et al., 2018; Li et al., 2018b; Tang et al., 2018a; Xu et al., 2018b; Xue et al., 2017; Ye et al., 2014; Zhang et al., 2018a, 2018c; Zhao et al., 2017b). Aiming to lower the E_{loss} and realize high performance of TZNT-based WBG polymers here, BDT derivatives with alkylthiothienyl group and fluorinated alkylthiothienyl side chains were selected as the donor blocks. As expected, these two copolymers exhibited a band gap approaching 2.0 eV, which could enable complementary absorption to those excellent LBG acceptors. The HOMO level lowered from −5.39 eV for PBDTS-TZNT to −5.45 eV for PBDTS-TZNT by introducing sulfur atoms or both sulfur and fluorine atoms. Such low HOMO level of PBDTSF-TZNT contributed a very large V_{oc} of 0.98 V if using 3,9-bis(2-methylene-(3-(1,1-dicyanomethylene)-indanone)-5,5,11,11-tetrakis(4-hexylphenyl)-dithieno[2,3-d:2′,3′-d′]-s-indaceno[1,2-b:5,6-b′]-dithiophene (ITIC) as the acceptor, leading to low E_{loss} of 0.61 V and high PCE of 12.16%. Moreover, the large V_{oc} of 0.93 V could be maintained even using 3,9-bis(2-methylene-(5,6-difluoro-(3-(1,1-dicyanomethylene)-indanone)-5,5,11,11-tetrakis(4-hexylphenyl)-dithieno[2,3-d:2′,3′-d′]-s-indaceno[1,2-b:5,6-b′]-dithiophene (IT-4F) acceptor with a much lower lowest unoccupied molecular orbital (LUMO) level (−3.99 eV) (Zhang et al., 2018c), which further lowered the E_{loss} to 0.59 eV and improved the PCE up to 13.25%. To further enhance the light-harvesting ability and elevate the device performance, homo-tandem devices containing two PBDTSF-TZNT:IT-4F-based subcells were fabricated. The resulting tandem devices displayed a very high PCE of 14.52% with a V_{oc} of 1.82 V, a short current density (J_{sc}) of 11.58 mA cm^{-2}, and a fill factor (FF) of 68.9%, which is the best record for homo-tandem NF-PSCs reported at present.

RESULTS AND DISCUSSION

The synthetic routes of the intermediates and target copolymers are shown in Scheme 1. Their detailed synthesis procedures are provided in the Supplemental Information. The organic tin monomers (M2 and M3) and naphtha[1,2-c:5,6-c]bis(1H-[1,2,3]triazole) (compound 1) were synthesized according to previous procedures (Dong et al., 2013; Zhang et al., 2018a). Compound 3 was synthesized by alkylation of compound 1 and bromination of compound 2. Compound M1 was synthesized by Stille coupling of compound 3 with tributyl(4-(2-butyloctyl)thiophen-2-yl)stannane then followed by bromination. The target copolymers of

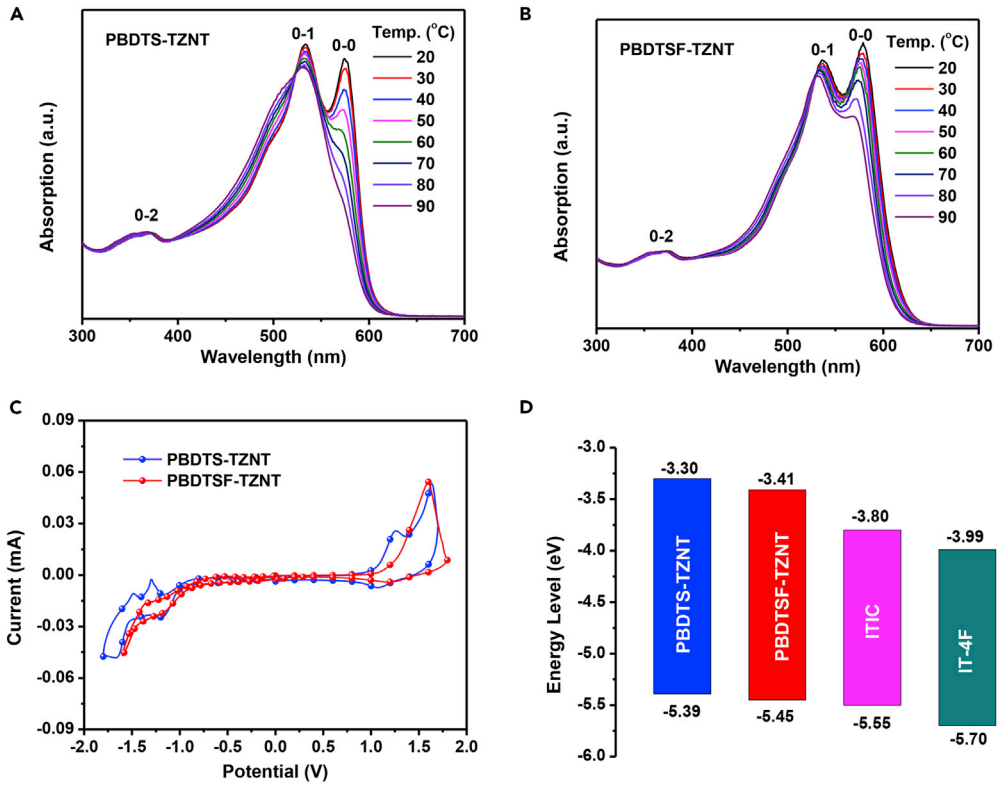

Figure 2. Absorption and Energy Level Comparison of Copolymer Donors and Acceptors

(A) The temperature-dependent absorption of PBDTS-TZNT in CB solution.

(B) The temperature-dependent absorption of PBDTSF-TZNT in CB solution

(C) Cyclic voltammogram curves of PBDTS-TZNT and PBDTSF-TZNT.

(D) Energy level diagram of the donor and acceptor materials.

Also see Figures S2 and S3.

PBDTS-TZNT and PBDTSF-TZNT were synthesized by Stille coupling polymerization using $Pd_2(dba)_3$/P(*o*-tolyl)$_3$ as catalyst in good yields. The intermediates and the final products were characterized by nuclear magnetic resonance spectroscopy and elemental analysis. Both copolymers have good solubility in common organic solvents, such as chloroform (CF), toluene, chlorobenzene (CB), and *o*-dichlorobenzene. The number average molecular weights (M_ns) were 43.1 and 44.5 kDa, and the polydispersity indices were 2.48 and 2.51 for PBDTS-TZNT and PBDTSF-TZNT, respectively, determined by gel permeation chromatography. The decomposition temperatures (T_ds, 5% weight loss) were 343°C and 356°C for PBDTS-TZNT and PBDTSF-TZNT, respectively, showing their good thermal stabilities (Figure S1A). Differential scanning calorimetry experiments displayed no obvious endothermal and exothermal peaks from room temperature to 300°C (Figure S1B), which might be due to the rigid backbones of the copolymers that limited the chain motion (Osaka et al., 2012).

Figures 2A and 2B showed the ultraviolet-visible absorption spectra of these two copolymers in CB solution at different temperatures. Both copolymers displayed similar absorption profiles with an obvious peak shoulder at room temperature due to their identical backbones. The 0-0, 0-1, and 0-2 peaks were assigned to the inter-, intramolecular, and π-π* transitions, respectively (Wan et al., 2017). Compared with PBDTS-TZNT, the slightly red-shifted 0-0 (579 versus 574 nm) and 0-1 (536 versus 533 nm) peaks demonstrated stronger molecular aggregation. Also, this was further examined by increasing the solution temperature. The peak 0-0 peak of PBDTS-TZNT decreased sharply with increasing the temperature, and almost disappeared at high temperature. However, such peak shoulder could be still observed in PBDTSF-TZNT solution even at 90°C. The stronger aggregation of PBDTSF-TZNT would help to enhance the absorption and crystallinity. In film states, the 0-0 and 0-1 peaks were 576 and 537 nm for PBDTS-TZNT and 582 and 540 nm for PBDTSF-TZNT, respectively (Figure 1B). Compared with their solution counterparts, the red-shifted

Copolymer	Solution	Film	E_g^{opt} (eV)	HOMO (eV)	LUMO (eV)	E_g^{CV} (eV)
	λ_{peak} (nm)	λ_{peak} (nm)				
PBDTS-TZNT	533,575	537.576	1.99	−5.39	−3.30	2.09
PBDTSF-TZNT	536,579	540,582	1.97	−5.45	−3.41	2.04

Table 1. Optical and Electrochemical Properties of the Copolymers

absorption indicated that the molecular packing was enhanced in film state. The maximum absorption coefficient was 8.54×10^4 cm^{-1} (537 nm) for PBDTS-TZNT and 1.12×10^5 cm^{-1} (540 nm) for PBDTSF-TZNT, respectively (Figure 1B). In contrast, J50, which incorporated the BTA block, exhibited a much lower maximum absorption coefficient of 6.79×10^4 cm^{-1} (Figure 1B). J91 with both fluorination on the BTA skeleton and the conjugated side chains of BDT showed a much higher absorption coefficient (0.98×10^5 cm^{-1}) than J50, but still lower than our newly prepared copolymer of PBDTSF-TZNT (Xue et al., 2017). The stronger absorption of PBDTSF-TZNT would be beneficial for harvesting more photons in devices. The optical band gaps (E_g^{opt}s) of PBDTS-TZNT and PBDTSF-TZNT were 1.99 and 1.97 eV, respectively, which could form good complementary absorption with typical LBG NFAs, such as ITIC and IT-4F (Figures 1B and S2). The optical characteristics of the copolymers are summarized in Table 1.

Cyclic voltammogram was employed to estimate the energy levels of the copolymers (Figure 2C). The HOMO/LUMO levels of PBDTS-TZNT and PBDTSF-TZNT were −5.39/-3.30 and −5.45/-3.41 eV, respectively, which matched well with ITIC and IT-4F acceptors (Figure 2D) (Zhang et al., 2018c). The lower-lying HOMO level of PBDTSF-TZNT could be expected to obtain higher V_{oc} in devices (Figure 1C). Moreover, the very low HOMO offset between PBDTSF-TZNT and ITIC (0.07 eV) or IT-4F (0.22 eV) could also be beneficial for reducing the E_{loss} to further increase V_{oc}. Density functional theory calculations were performed at the B3LYP/6-31G(d) level to investigate the electronic structures of these two copolymers. As shown in Figure S3, the fluorinated side chains on PBDTSF-TZNT showed a smaller dihedral angle of 53.7° than that of PBDTSF-TZNT (54.1°) in the ground state, which agreed well with the absorption differences as discussed above. The densities of their HOMOs were more populated on the BDT segments, whereas the LUMOs were mainly distributed over the TZNT skeletons. The HOMO/LUMO levels of PBDTS-TZNT and PBDTSF-TZNT were calculated to be −4.76/-2.51 and −4.85/-2.61 eV, respectively, which agreed well with the electrochemical results, indicating that fluorination could efficiently lower the energy levels but had less effect on the band gaps.

The photovoltaic properties of the two donor copolymers were investigated by using an inverted device of glass/indium tin oxide (ITO)/ZnO/copolymer:ITIC or IT-4F/MoO_3/Al. The optimization conditions included the donor/acceptor ratios, solvents, concentrations, solvent additives, and thermal annealing (TA) treatments (Figures S4–S10, Tables S1–S3). The optimized condition was determined to be 1:1 (w/w) with 0.2 v/v% of 1,8-diiodoethane and a total concentration of 14 mg mL^{-1} in CF solution. TA treatment of the as-cast film at 100°C for 5 min before electrode deposition could further optimize blend morphology and improve the device performance. As shown in Figure 3 and Table 2, using ITIC as the acceptor, PBDTS-TZNT-based devices showed a PCE of 10.45% with a V_{oc} of 0.94 V, a J_{sc} of 16.92 mA cm^{-2}, and an FF of 65.7%. A simultaneously improved V_{oc} of 0.98 V, J_{sc} of 17.57 mA cm^{-2}, and FF of 70.6% yielded a higher PCE of 12.16% for PBDTSF-TZNT devices, owing to the lower energy level, higher absorption, and more compact molecular packing of PBDTSF-TZNT. The E_{loss} would be decreased from 0.65 eV for PBDTS-TZNT:ITIC to 0.61 eV for PBDTSF-TZNT:ITIC, which were relatively low among those devices based on BTA-containing donor copolymers. However, the PCEs were still limited by J_{sc} and FF, which might be partly due to the limited absorption range and small HOMO offset. Bearing this in mind, IT-4F with a lower HOMO level and red-shifted absorption was selected instead of ITIC. As expected, the slightly decreased V_{oc}s were observed to be 0.88 for PBDTS-TZNT:IT-4F and 0.93 V for PBDTSF-TZNT:IT-4F devices, respectively. However, the relatively high V_{oc} of 0.93 V is still much higher than those of efficient NF-PSCs using IT-4F as the acceptor (Li et al., 2018a; Zhang et al., 2018d; Zheng et al., 2018), thus leading to a very low E_{loss} of 0.59 eV. Nevertheless, such low E_{loss} would not restrict the corresponding charge extraction process. High J_{sc} of 19.23 mA cm^{-2} and FF of 74.1% were obtained for PBDTSF-TZNT:IT-4F devices, giving rise to the best PCE of 13.25%. On the other hand, slightly reduced E_{loss} of 0.64 eV and obviously improved PCE of 11.31% could be also achieved in PBDTS-TZNT:IT-4F devices. The above-mentioned

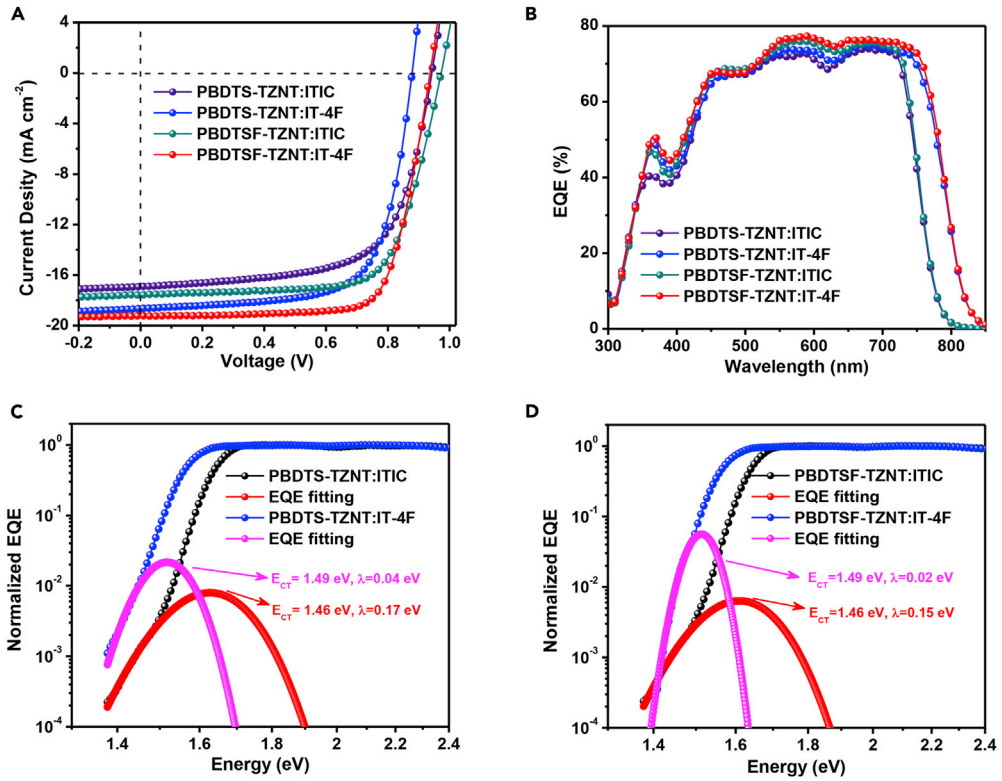

Figure 3. Device Performance of Binary Blend NF-PSCs

(A) *J-V* curves of the binary blend NF-PSCs.

(B) EQE curves of the binary blend NF-PSCs.

(C) The normalized EQE_{PV} spectra in logarithmic scale of PBDTS-TZNT-based binary blend devices.

(D) The normalized EQE_{PV} spectra in logarithmic scale of PBDTSF-TZNT-based binary blend devices.

Also see Figures S4–S10 and Tables S1–S3.

device performance improvements were confirmed by the external quantum efficiency (EQE) evaluations (Figure 3B). PSCs based on IT-4F displayed higher and broader photoresponse (300–825 nm) than the ITIC-based devices (300–800 nm). Clearly, PBDTSF-TZNT devices exhibited higher photoresponse than PBDTS-TZNT devices. These were reasonable due to the higher absorptions of IT-4F and PBDTSF-TZNT. The calculated current densities (J_{EQE}) were 16.36 and 17.22 mA cm^{-2} for PBDTS-TZNT and PBDTSF-TZNT devices using ITIC acceptor, respectively, and these were enhanced to 18.63 and 18.97 mA cm^{-2} if using IT-4F acceptor. The calculated results matched well with those values obtained from *J-V* measurements.

To gain insight into the low E_{loss} in this work, the charge transfer state energy (E_{CT}) and reorganization energy (λ) were explored. E_{CT} and λ were extracted from Equation 1 according to Marcus theory (Marcus, 1989; Zhao et al., 2016).

Active Layer	V_{oc} (V)	J_{sc} (mA cm^{-2})	J_{EQE}[b] (mA cm^{-2})	FF (%)	PCE (%)
PBDTS-TZNT:ITIC	0.94 (0.93 ± 0.01)[a]	16.92 (16.79 ± 0.13)	16.45	65.7 (64.9 ± 0.8)	10.45 (10.13 ± 0.32)
PBDTS-TZNT:IT-4F	0.88 (0.87 ± 0.01)	18.65 (18.54 ± 0.11)	18.23	68.9 (68.2 ± 0.7)	11.31 (11.00 ± 0.31)
PBDTSF-TZNT:ITIC	0.98 (0.97 ± 0.01)	17.58 (17.49 ± 0.09)	17.22	70.6 (69.6 ± 1.0)	12.16 (11.81 ± 0.35)
PBDTSF-TZNT:IT-4F	0.93 (0.92 ± 0.01)	19.23 (19.13 ± 0.10)	18.97	74.1 (73.4 ± 0.7)	13.25 (12.92 ± 0.33)

Table 2. Photovoltaic Parameters of the NF-PSCs

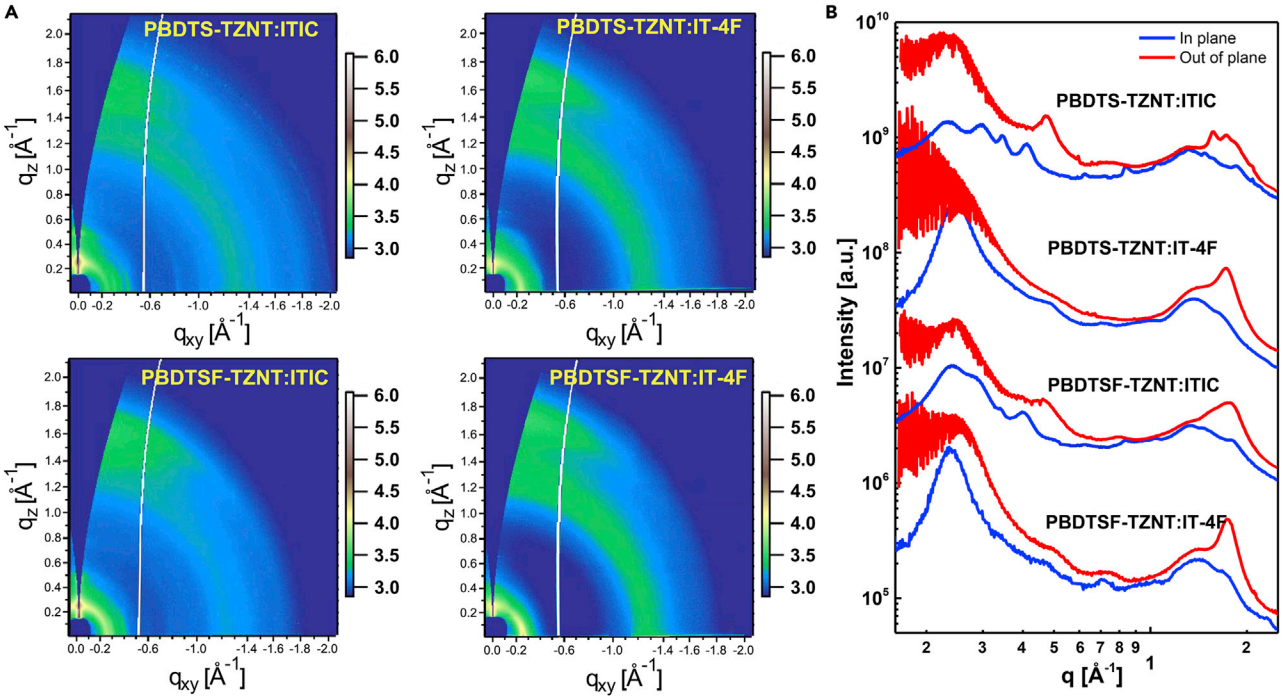

Figure 4. GIWAXS Analysis of Blend Films

(A) GIWAXS patterns of PBDTS-TZNT:ITIC, PBDTS-TZNT:IT-4F, PBDTSF-TZNT:ITIC, and PBDTSF-TZNT:IT-4F blend films.

(B) In-plane and out-of-plane line-cut profiles of PBDTS-TZNT:ITIC, PBDTS-TZNT:IT-4F, PBDTSF-TZNT:ITIC, and PBDTSF-TZNT:IT-4F blend films.

Also see Figure S11 and Table S4.

$$EQE_{PV}(E) = \frac{f}{E\sqrt{4\pi\lambda kT}} exp\left(\frac{-(E_{CT}+\lambda-E)^2}{4\lambda kT}\right) \quad \text{(Equation 1)}$$

where EQE_{PV} represents the photovoltaic EQE, f is proportional to the absorption strength of the charge transfer state and the density of the donor/acceptor interfaces, λ represents the reorganized energy of the charge transfer states, and E represents the photon energy. As shown in Figures 3C and 3D, using ITIC as the acceptor, the E_{CT} was 1.46 eV for both devices. Thus the energy losses resulting from charge transfer (E_g−E_{CT}) was 0.13 eV. However, the λ reduced from 0.17 eV (PBDTS-TZNT:ITIC) to 0.15 eV (PBDTSF-TZNT:ITIC). The lower reorganization energy indicated the less energetic disorder of charge transfer states, leading to a smaller voltage deficit in PBDTSF-TZNT:ITIC devices (Xiao et al., 2018). Moreover, using IT-4F as the acceptor, the E_{CT} increased to 1.49 eV for both devices, resulting in the lower E_g-E_{CT} of 0.03 eV. In the meantime, λ further reduced to 0.04 eV for PBDTS-TZNT:IT-4F and to 0.02 eV for PBDTSF-TZNT:IT-4F devices. Therefore, the lowest E_g−E_{CT} and λ values of PBDTS-TZNT:IT-4F blend contributed to the smallest E_{loss} in the resulting devices.

To gain in-depth structural information on the molecular packing behaviors, 2D grazing incidence wide-angle X-ray scattering was performed (Figures 4 and S11 and Table S4). The neat PBDTS-TZNT and PBDTSF-TZNT films exhibited (100) diffraction peak at q_{xy} = 0.25 Å^{-1}, corresponding to their lamellar stacking distance (d_L) of 25.1 Å, which was due to their identical alkyl side chains. However, PBDTSF-TZNT film displayed a smaller π-π stacking distance (d_π) of 3.61 Å (q_z = 1.74 Å^{-1}) and a larger coherent length (L_C) of 25 Å than PBDTS-TZNT (3.63 Å, q_z = 1.73 Å^{-1}, L_C = 23 Å). The results indicated that the more ordered molecular packing of PBDTSF-TZNT was formed, owing to the introduced noncovalent effect by fluorination. After blending with ITIC, their high crystallinities were lowered to some extent, along with the reduced L_Cs of 16 and 22 Å for PBDTS-TZNT:ITIC and PBDTSF-TZNT:ITIC, respectively. The PBDTS-TZNT:ITIC blend exhibited much stronger (100) diffraction along the q_z direction than the q_{xy} direction, indicating its more preferred edge-on packing. However, a more balanced coexistence of face-on and edge-on packing of PBDTSF-TZNT:ITIC was observed to enable the more efficient three-dimensional charge transfer. If using IT-4F instead of ITIC, significantly improved diffractions were observed with the increased L_Cs of 26 and

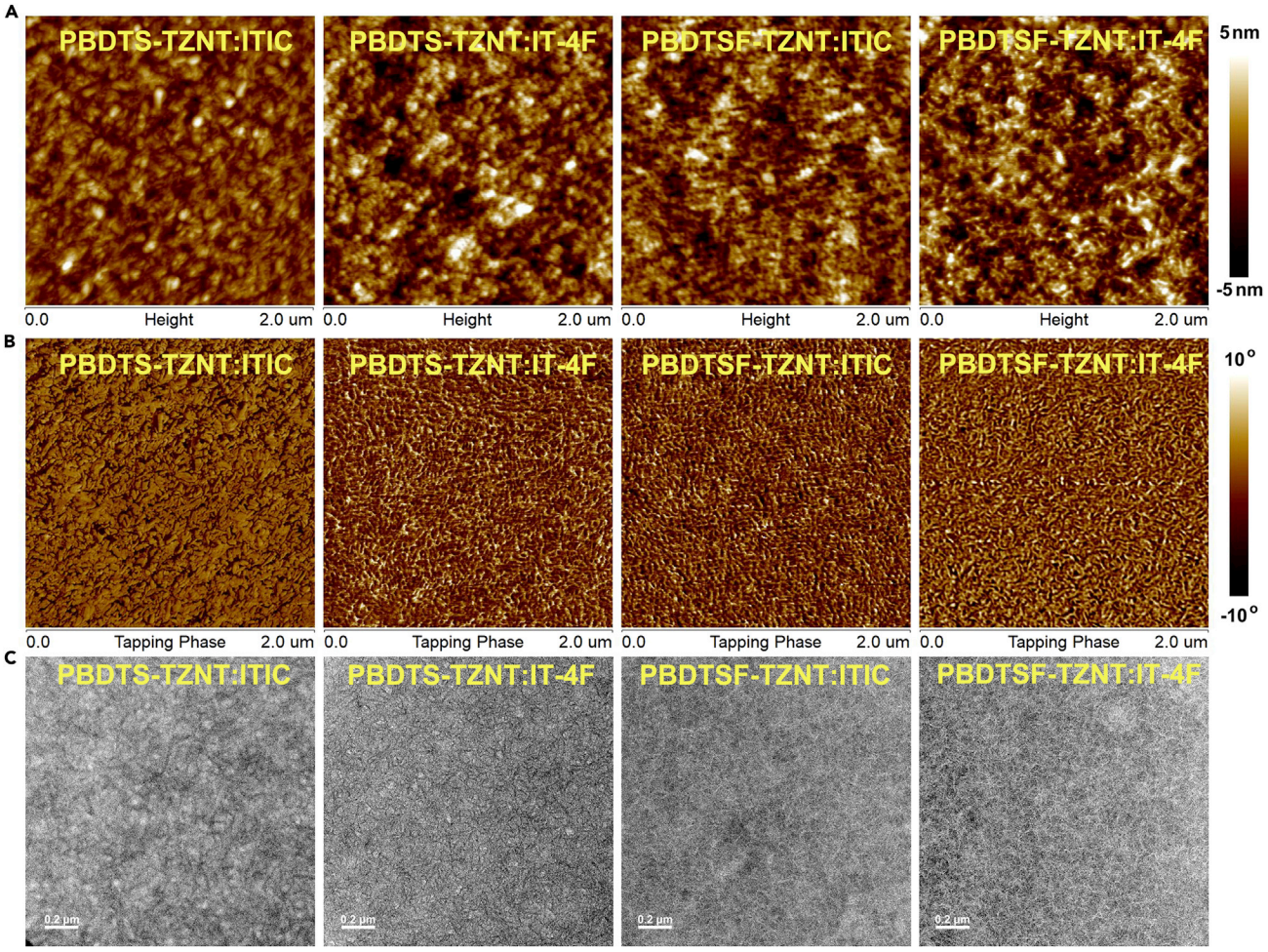

Figure 5. Analysis of the Morphology of Blend Films

(A) Atomic force microscopy (AFM) height images of PBDTS-TZNT:ITIC, PBDTS-TZNT:IT-4F, PBDTSF-TZNT:ITIC, and PBDTSF-TZNT:IT-4F blend films.

(B) AFM phase images of PBDTS-TZNT:ITIC, PBDTS-TZNT:IT-4F, PBDTSF-TZNT:ITIC, and PBDTSF-TZNT:IT-4F blend films.

(C) Transmission electron microscopic (images) of PBDTS-TZNT:ITIC, PBDTS-TZNT:IT-4F, PBDTSF-TZNT:ITIC, and PBDTSF-TZNT:IT-4F blend films.

Also see Figure S13.

30 Å for PBDTS-TZNT:IT-4F and PBDTSF-TZNT:IT-4F, respectively, showing their enhanced crystallinities. Moreover, both blends showed stronger (100) diffraction along the q_{xy} direction than the q_z directions, indicating that more preferred face-on packing was realized. Such stacking change would be positive for vertical charge transfer in PSC devices. The hole mobility (μ_h) and electron mobility (μ_e) of the blend films were estimated by space-charge-limited current method (Figure S12). The μ_h/μ_e of PBDTS-TZNT:ITIC, PBDTS-TZNT:IT-4F, PBDTSF-TZNT:ITIC, and PBDTS-TZNT:IT-4F blends were measured to be $1.04 \times 10^{-4}/3.26 \times 10^{-5}$, $2.65 \times 10^{-4}/1.26 \times 10^{-4}$, $3.21 \times 10^{-4}/1.87 \times 10^{-4}$, and $5.10 \times 10^{-4}/4.03 \times 10^{-4}$ cm^2 V^{-1} s^{-1}, respectively. As could be concluded, the improved crystallinity promoted by fluorination on the conjugated side chains of donor polymer and the end group of the acceptor would benefit the charge carrier mobilities. Finally, the highest and most balanced μ_h/μ_e ratio of PBDTS-TZNT:IT-4F correlated to the highest J_{sc} and FF values in the related NF-PSCs.

Resonant soft X-ray scattering (RSoXS) experiments were carried out to study the nanophase separation and the average composition distribution of the blend films (Figure S13). The PBDTS-TZNT:ITIC blend exhibited relatively low scattering intensity with two peaks located at 0.03 and 0.12 nm^{-1}, respectively, corresponding to the large domain sizes of 105 and 26 nm, showing the non-uniform nanophase separation. Higher scattering intensity with slightly reduced domain size of 24 nm was observed for the PBDTSF-TZNT:ITIC blend, showing the improved domain purity and better morphology. If replacing ITIC with

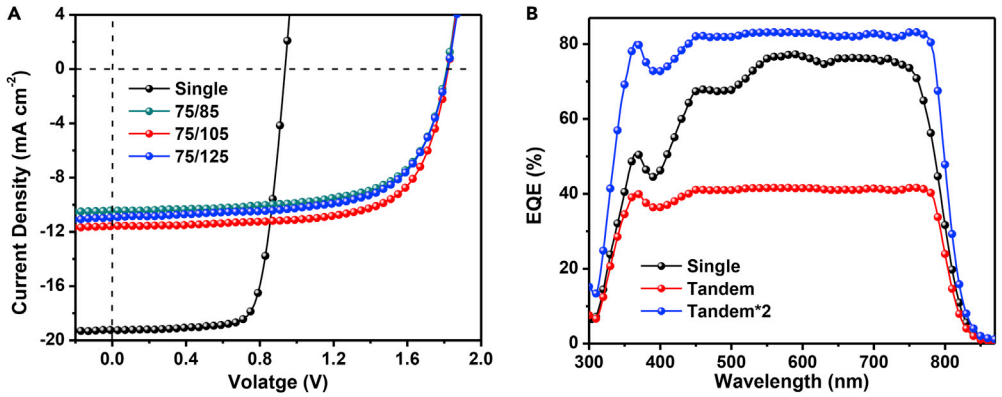

Figure 6. Device Performance of Homo-Tandem Cells

(A) *J-V* curves of the single-junction and homo-tandem devices based on PBDTSF-TZNT:IT-4F blend layer.

(B) EQE curves of the single-junction and homo-tandem devices based on PBDTSF-TZNT:IT-4F blend layer.

Also see Figure S14.

IT-4F, both polymer blends exhibited significantly improved scattering intensity with further reduced domain sizes of 24 nm for PBDTS-TZNT:IT-4F and 18 nm for PBDTSF-TZNT:IT-4F. This was due to the faster crystallization of IT-4F-based blends during the film deposition. The phase separation could be visually observed by atomic force microscopy and transmission electron microscopy (Figure 5). PBDTS-TZNT:ITIC appeared to have a fairly smooth top surface with a root-mean-square (RMS) roughness of 0.78 nm. The coexistence of large and small domains could be observed, which agreed well with the RSoXS results. Gradually increasing RMS values of 1.14, 1.45, and 1.53 nm with more fibril-like interpenetrating networks could be observed in PBDTSF-TZNT:ITIC and PBDTS-TZNT:IT-4F blends. The better nanofibril domains in PBDTSF-TZNT:IT-4F with the highest domain purity provided the most efficient exciton dissociation and charge transfer for realizing the best device performance.

Although high PCEs had been achieved in single-junction NF-PSCs, the device performance was still limited by incomplete light harvesting. To make full use of sunlight and further increase the device performance, homo-tandem cells were fabricated and evaluated with the device configuration of glass/ITO/ZnO/PBDTSF-TZNT:IT-4F/PEDOT:PSS/ultrathin Ag/ZnO/PBDTSF- TZNT:IT-4F/MoO_3/Ag. To get enough high PCE, the active layer thickness of the bottom cell was determined to be 75 nm and thickness of the top cell ranged from 85 to 125 nm (Figure 6 and Table 3). When the thickness of the top cell was 105 nm, the resulting devices exhibited the best PCE of 14.52% with a V_{oc} of 1.82 V, a J_{sc} of 11.58 mA cm^{-2}, and an FF of 68.9%. The device performance was certified by a third party as a PCE of 14.14% (Figure S14). To the best of our knowledge, this is a new record for homo-tandem PSCs. On the other hand, over 80% of the original device performance could be retained after storing in the glove box for 300 h (Figure S15). The EQE spectra confirmed the improved light-harvesting ability (Figure 6B). The EQE of the homo-tandem device here is defined as the ratio of the total converted carriers by the two subcells to the sum of the incident photons and is estimated by measuring the photoresponse of the tandem cell and then multiplying it by 2 to represent the total number of photons being converted to electrons (Xu et al., 2018b). The fabricated homo-tandem devices displayed high EQE response of around 40% from 450 to 750 nm with a highest value of 41.5%. Thus the total EQE response of the homo-tandem solar cells reached 83% on superposition of two subcells. The calculated J_{EQE} was 11.27 mA cm^{-2}, which agreed well with the *J-V* result.

Film Thickness (nm)	V_{oc} (V)	J_{sc} (mA cm^{-2})	FF (%)	PCE (%)
75/85	1.81 (1.79 ± 0.02)	10.43 (10.28 ± 0.15)	66.7 (65.4 ± 1.3)	12.59 (12.04 ± 0.55)
75/105	1.82 (1.80 ± 0.02)	11.58 (11.47 ± 0.11)	68.9 (67.9 ± 1.0)	14.52 (14.02 ± 0.50)
75/125	1.81 (1.79 ± 0.02)	10.95 (10.81 ± 0.14)	65.9 (64.5 ± 1.4)	13.06 (12.48 ± 0.58)

Table 3. Photovoltaic Parameters of the Homo-Tandem NF-PSCs

The averaged photovoltaic parameters in parentheses were obtained from at least 15 devices.

Also see Figure S15.

Conclusions

Two novel TZNT-containing WBG polymers, PBDTS-TZNT and PBDTSF-TZNT, were successfully designed and synthesized for highly efficient NF-PSCs with low energy loss. The rigid planar backbone of BDT and TZNT units provided these copolymers with high crystallinity and good molecular packing. Sulfuration and fluorination side chains of BDT lowered the HOMO level (5.39 eV for PBDTS-TZNT and −5.45 eV for PBDTSF-TZNT) for guaranteeing high V_{oc} up to 0.98 V using ITIC as the acceptor. If selecting IT-4F instead of ITIC, the relatively low E_{loss} of 0.59 eV would be realized even keeping the high V_{oc} of 0.93 V. Beside this, broadened absorption, better matched energy level, further improved crystallinity, and fine-tuned morphology enabled PBDTSF-TZNT-based devices to promote the PCE from 12.16% to 13.25%. Moreover, to make full use of sunlight, homo-tandem devices based on PBDTSF-TZNT:IT-4F were fabricated and evaluated, which exhibited the highest PCE of 14.52% with a V_{oc} of 1.82 V, a J_{sc} of 11.58 mA cm^{-2}, and an FF of 68.9%. This work demonstrated that fine-tuning the electronic energy level and molecular packing of WBG donor copolymers and pairing them with a proper LBG acceptor is a promising way to realize high efficiency and low energy loss at the same time in NF-PSCs.

METHODS

All methods can be found in the accompanying Transparent Methods supplemental file.

SUPPLEMENTAL INFORMATION

Supplemental Information includes Transparent Methods, 15 figures, and 4 tables and can be found with this article online at https://doi.org/10.1016/j.isci.2018.12.027.

ACKNOWLEDGMENTS

The authors acknowledge financial support from NSFC (21825502, 51573107, 91633301, and 21432005) and the Foundation of State Key Laboratory of Polymer Materials Engineering (sklpme2017-2-04).

AUTHOR CONTRIBUTIONS

Q.P. proposed the research and directed the study. K.F. synthesized and characterized the polymer donor materials. X.X. and G.Z. helped with the device fabrication and characterization. J.Y. Z.B. and W.M. performed the GIWXAS and RSoXS characterization and analyzed the data. X.X. and Q.P. prepared the manuscript. All authors discussed the results and commented on the manuscript.

DECLARATION OF INTERESTS

The authors declare no competing interests.

Received: October 30, 2018
Revised: December 12, 2018
Accepted: December 24, 2018
Published: February 22, 2019

REFERENCES

Bin, H.J., Gao, L., Zhang, Z.G., Yang, Y.K., Zhang, Y.D., Zhang, C.F., Chen, S.S., Xue, L.W., Yang, C., Xiao, M., and Li, Y.F. (2016a). 11.4% Efficiency non-fullerene polymer solar cells with trialkylsilyl substituted 2D-conjugated polymer as donor. Nat. Commun. *7*, 13651.

Bin, H.J., Zhang, Z.G., Gao, L., Chen, S.S., Zhong, L., Xue, L.W., Yang, C., and Li, Y.F. (2016b). Non-fullerene polymer solar cells based on alkylthio and fluorine substituted 2D-conjugated polymers reach 9.5% efficiency. J. Am. Chem. Soc. *138*, 4657–4664.

Cai, Y.H., Huo, L.J., and Sun, Y.M. (2017). Recent advances in wide-bandgap photovoltaic polymers. Adv. Mater. *29*, https://doi.org/10.1002/adma.201605437.

Cheng, Y.-J., Yang, S.-H., and Hsu, C.-S. (2009). Synthesis of conjugated polymers for organic solar cell applications. Chem. Rev. *109*, 5868–5923.

Cui, Y., Yao, H.F., Gao, B.W., Qin, Y.P., Zhang, S.Q., Yang, B., He, C., Xu, B.W., and Hou, J.H. (2017). Fine-tuned photoactive and interconnection layers for achieving over 13% efficiency in a fullerene-free tandem organic solar cell. J. Am. Chem. Soc. *139*, 7302–7309.

Dong, Y., Hu, X.W., Duan, C.H., Liu, P., Liu, S.J., Lan, L.Y., Chen, D.C., Ying, L., Su, S.J., Gong, X., et al. (2013). A series of new medium-bandgap conjugated polymers based on naphtho[1,2-c:5,6-c]bis(2-octyl-[1,2,3]triazole) for high-performance polymer solar cells. Adv. Mater. *25*, 3683–3688.

Fan, Q.P., Su, W.Y., Meng, X.Y., Guo, X., Li, G.D., Ma, W., Zhang, M.J., and Li, Y.F. (2017). High-performance non-fullerene polymer solar cells based on fluorine substituted wide bandgap copolymers without extra treatments. Solar RRL *1*, 1700020.

Fan, Q.P., Su, W.Y., Wang, Y., Guo, B., Jiang, Y.F., Guo, X., Liu, F., Russell, T.P., Zhang, M.J., and Li, Y.F. (2018). Synergistic effect of fluorination on both donor and acceptor materials for high performance non-fullerene polymer solar cells with 13.5% efficiency. Sci. Chin. Chem. *61*, 531–537.

Fei, Z.P., Eisner, F.D., Jiao, X.C., Azzouzi, M., Rohr, J.A., Han, Y., Shahid, M., Chesman, A.S.R., Easton, C.D., McNeill, C.R., et al. (2018). An

alkylated indacenodithieno[3,2-b]thiophene-based nonfullerene acceptor with high crystallinity exhibiting single junction solar cell efficiencies greater than 13% with low voltage losses. Adv. Mater. *30*, e1800728.

Lan, L.Y., Zhang, G.C., Dong, Y., Ying, L., Huang, F., and Cao, Y. (2015). Novel medium band gap conjugated polymers based on naphtho[1,2-c:5,6-c]bis[1,2,3]triazole for polymer solar cells. Polymer *67*, 40–46.

Li, G., Zhu, R., and Yang, Y. (2012). Polymer solar cells. Nat. Photon. *6*, 153–161.

Li, S.S., Ye, L., Zhao, W.C., Zhang, S.Q., Mukherjee, S., Ade, H., and Hou, J.H. (2016). Energy-level modulation of small-molecule electron acceptors to achieve over 12% efficiency in polymer solar cells. Adv. Mater. *28*, 9423–9429.

Li, S.S., Ye, L., Zhao, W.C., Yan, H.P., Yang, B., Liu, D.L., Li, W.N., Ade, H., and Hou, J.H. (2018a). A wide band gap polymer with a deep highest occupied molecular orbital level enables 14.2% efficiency in polymer solar cells. J. Am. Chem. Soc. *140*, 7159–7167.

Li, W.W., Furlan, A., Hendriks, K.H., Wienk, M.M., and Janssen, R.A. (2013). Efficient tandem and triple-junction polymer solar cells. J. Am. Chem. Soc. *135*, 5529–5532.

Li, Z.J., Xu, X.P., Zhang, G.J., Yu, T., Li, Y., and Peng, Q. (2018b). Highly efficient non-fullerene polymer solar cells enabled by wide bandgap copolymers with conjugated selenyl side chains. Solar RRL *2*, 1800186.

Lin, Y.Z., Wang, J.Y., Zhang, Z.-G., Bai, H.T., Li, Y.F., Zhu, D.B., and Zhan, X.W. (2015a). An electron acceptor challenging fullerenes for efficient polymer solar cells. Adv. Mater. *27*, 1170–1174.

Lin, Y.Z., Zhang, Z.-G., Bai, H.T., Wang, J.Y., Yao, Y.H., Li, Y.F., Zhu, D.B., and Zhan, X.W. (2015b). High-performance fullerene-free polymer solar cells with 6.31% efficiency. Energy Environ. Sci. *8*, 610–616.

Lin, Y.Z., and Zhan, X.W. (2016). Oligomer molecules for efficient organic photovoltaics. Acc. Chem. Res. *49*, 175–183.

Lin, Y.Z., Zhao, F.W., He, Q., Huo, L.J., Wu, Y., Parker, T.C., Ma, W., Sun, Y.M., Wang, C.R., Zhu, D.B., et al. (2016). High-performance electron acceptor with thienyl side chains for organic photovoltaics. J. Am. Chem. Soc. *138*, 4955–4961.

Lin, Y.Z., Zhao, F.W., Prasad, S.K.K., Chen, J.D., Cai, W.Z., Zhang, Q.Q., Chen, K., Wu, Y., Ma, W., Gao, F., et al. (2018). Balanced partnership between donor and acceptor components in nonfullerene organic solar cells with >12% efficiency. Adv. Mater. *30*, 1706363.

Liu, W.R., Zhang, J.Y., Zhou, Z.C., Zhang, D.Y., Zhang, Y., Xu, S.J., and Zhu, X.Z. (2018). Design of a new fused-ring electron acceptor with excellent compatibility to wide-bandgap polymer donors for high-performance organic photovoltaics. Adv. Mater. *30*, 1800403.

Luo, Z.H., Bin, H.J., Liu, T., Zhang, Z.G., Yang, Y.K., Zhong, C., Qiu, B.B., Li, G.H., Gao, W., Xie, D.J., et al. (2018). Fine-tuning of molecular packing and energy level through methyl substitution enabling excellent small molecule acceptors for nonfullerene polymer solar cells with efficiency up to 12.54. Adv. Mater. *30*, 1706124.

Marcus, R.A. (1989). Relation between charge transfer absorption and fluorescence spectra and the inverted region. J. Phys. Chem. *93*, 3078–3086.

Meng, L.X., Zhang, Y.M., Wan, X.J., Li, C.X., Zhang, X., Wang, Y.B., Ke, X., Xiao, Z., Ding, L.M., Xia, R.X., et al. (2018). Organic and solution-processed tandem solar cells with 17.3% efficiency. Science *361*, 1094–1098.

Min, J., Zhang, Z.G., Zhang, S.Y., Zhang, M.J., Zhang, J., and Li, Y.F. (2011). Synthesis and photovoltaic properties of D–A copolymers based on dithienosilole and benzotriazole. Macromolecules *44*, 7632–7638.

Min, J., Zhang, Z.G., Zhang, S.Y., and Li, Y.F. (2012). Conjugated side-chain-isolated D–A copolymers based on benzo[1,2-b:4,5-b′] dithiophene-alt-dithienylbenzotriazole: synthesis and photovoltaic properties. Chem. Mater. *24*, 3247–3254.

Osaka, I., Shimawaki, M., Mori, H., Doi, I., Miyazaki, E., Koganezawa, T., and Takimiya, K. (2012). Synthesis, characterization, and transistor and solar cell applications of a naphthobisthiadiazole-based semiconducting polymer. J. Am. Chem. Soc. *134*, 3498–3507.

Osaka, I., and Takimiya, K. (2017). Naphthobischalcogenadiazole conjugated polymers: Emerging materials for organic electronics. Adv. Mater. *29*, 1605218.

Price, S.C., Stuart, A.C., Yang, L.Q., Zhou, H.X., and You, W. (2011). Fluorine substituted conjugated polymer of medium band gap yields 7% efficiency in polymer-fullerene solar cells. J. Am. Chem. Soc. *133*, 4625–4631.

Shim, J.W., Zhou, Y.H., Fuentes-Hernandez, C., Dindar, A., Guan, Z.L., Cheun, H., Kahn, A., and Kippelen, B. (2012). Studies of the optimization of recombination layers for inverted tandem polymer solar cells. Sol. Energy Mater. Sol. C *107*, 51–55.

Tang, A.L., Xiao, B., Chen, F., Zhang, J.Q., Wei, Z.X., and Zhou, E.J. (2018a). The introduction of fluorine and sulfur atoms into benzotriazole-based p-type polymers to match with a benzotriazole-containing n-type small molecule: "The same-acceptor-strategy" to realize high open-circuit voltage. Adv. Energy Mater. *8*, 1801582.

Tang, D.S., Wan, J.H., Xu, X.P., Lee, Y.W., Woo, H.Y., Feng, K., and Peng, Q. (2018b). Naphthobistriazole-based wide bandgap donor polymers for efficient non-fullerene organic solar cells: significant fine-tuning absorption and energy level by backbone fluorination. Nano Energy *53*, 258–269.

Vasilopoulou, M., Polydorou, E., Douvas, A.M., Palilis, L.C., Kennou, S., and Argitis, P. (2015). Annealing-free highly crystalline solution-processed molecular metal oxides for efficient single-junction and tandem polymer solar cells. Energy Environ. Sci. *8*, 2448–2463.

Wan, J.H., Xu, X.P., Zhang, G.J., Li, Y., Feng, K., and Peng, Q. (2017). Highly efficient halogen-free solvent processed small-molecule organic solar cells enabled by material design and device engineering. Energy Environ. Sci. *10*, 1739–1745.

Wang, M., Hu, X.W., Liu, P., Li, W., Gong, X., Huang, F., and Cao, Y. (2011). Donor-acceptor conjugated polymer based on naphtho[1,2-c:5,6-c] bis[1,2,5]thiadiazole for high-performance polymer solar cells. J. Am. Chem. Soc. *133*, 9638–9641.

Xiao, J.Y., Chen, Z.M., Zhang, G.C., Li, Q.-Y., Yin, Q.W., Jiang, X.-F., Huang, F., Xu, Y.-X., Yip, H.-L., and Cao, Y. (2018). Efficient device engineering for inverted non-fullerene organic solar cells with low energy loss. J. Mater. Chem. C *6*, 4457–4463.

Xiao, Z., Jia, X., and Ding, L.M. (2017). Ternary organic solar cells offer 14% power conversion efficiency. Sci. Bull. *62*, 1562–1564.

Xu, X.P., Bi, Z.Z., Ma, W., Wang, Z.S., Choy, W.C.H., Wu, W.L., Zhang, G.J., Li, Y., and Peng, Q. (2017). Highly efficient ternary-blend polymer solar cells enabled by a nonfullerene acceptor and two polymer donors with a broad composition tolerance. Adv. Mater. *29*, 1704271.

Xu, X.P., Li, Z.J., Bi, Z.Z., Yu, T., Ma, W., Feng, K., Li, Y., and Peng, Q. (2018a). Highly efficient nonfullerene polymer solar cells enabled by a copper(I) coordination strategy employing a 1,3,4-oxadiazole-containing wide-bandgap copolymer donor. Adv. Mater. *30*, 1800737.

Xu, X.P., Yu, T., Bi, Z.Z., Ma, W., Li, Y., and Peng, Q. (2018b). Realizing over 13% efficiency in green-solvent-processed nonfullerene organic solar cells enabled by 1,3,4-thiadiazole-based wide-bandgap copolymers. Adv. Mater. *30*, https://doi.org/10.1002/adma.201703973.

Xue, L.W., Yang, Y.K., Xu, J.Q., Zhang, C.F., Bin, H.J., Zhang, Z.G., Qiu, B.B., Li, X.J., Sun, C.K., Gao, L., et al. (2017). Side chain engineering on medium bandgap copolymers to suppress triplet formation for high-efficiency polymer solar cells. Adv. Mater. *29*, https://doi.org/10.1002/adma.201703344.

Yan, C.Q., Barlow, S., Wang, Z.H., Yan, H., Jen, A.K.Y., Marder, S.R., and Zhan, X.W. (2018). Non-fullerene acceptors for organic solar cells. Nat. Rev. Mater. *3*, 18003.

Ye, L., Zhang, S.Q., Huo, L.J., Zhang, M.J., and Hou, J.H. (2014). Molecular design toward highly efficient photovoltaic polymers based on two-dimensional conjugated benzodithiophene. Acc. Chem. Res. *47*, 1595–1603.

Yu, T., Xu, X.P., Zhang, G.J., Wan, J.H., Li, Y., and Peng, Q. (2017). Wide bandgap copolymers based on quinoxalino[6,5-f]-quinoxaline for highly efficient nonfullerene polymer solar cells. Adv. Funct. Mater. *27*, 1701491.

Zhang, G.J., Xu, X.P., Bi, Z.Z., Ma, W., Tang, D.S., Li, Y., and Peng, Q. (2018a). Fluorinated and alkylthiolated polymeric donors enable both

efficient fullerene and nonfullerene polymer solar cells. Adv. Funct. Mater. *28*, 1706404.

Zhang, G.Y., Zhao, J.B., Chow, P.C.Y., Jiang, K., Zhang, J.Q., Zhu, Z.L., Zhang, J., Huang, F., and Yan, H. (2018b). Nonfullerene acceptor molecules for bulk heterojunction organic solar cells. Chem. Rev. *118*, 3447–3507.

Zhang, H., Yao, H.F., Hou, J.X., Zhu, J., Zhang, J.Q., Li, W.N., Yu, R.N., Gao, B.W., Zhang, S.Q., and Hou, J.H. (2018c). Over 14% efficiency in organic solar cells enabled by chlorinated nonfullerene small-molecule acceptors. Adv. Mater. *30*, e1800613.

Zhang, S.Q., Qin, Y.P., Zhu, J., and Hou, J.H. (2018d). Over 14% efficiency in polymer solar cells enabled by a chlorinated polymer donor. Adv. Mater. *30*, e1800868.

Zhao, F.W., Dai, S.X., Wu, Y., Zhang, Q.Q., Wang, J.Y., Jiang, L., Ling, Q.D., Wei, Z.X., Ma, W., You, W., et al. (2017a). Single-junction binary-blend nonfullerene polymer solar cells with 12.1% efficiency. Adv. Mater. *29*, https://doi.org/10.1002/adma.201700144.

Zhao, W.C., Qian, D.P., Zhang, S.Q., Li, S.S., Inganas, O., Gao, F., and Hou, J.H. (2016). Fullerene-free polymer solar cells with over 11% efficiency and excellent thermal stability. Adv. Mater. *28*, 4734–4739.

Zhao, W.C., Li, S.S., Yao, H.F., Zhang, S.Q., Zhang, Y., Yang, B., and Hou, J.H. (2017b). Molecular optimization enables over 13% efficiency in organic solar cells. J. Am. Chem. Soc. *139*, 7148–7151.

Zhao, W.C., Zhang, S.Q., Zhang, Y., Li, S.S., Liu, X.Y., He, C., Zheng, Z., and Hou, J.H. (2018). Environmentally friendly solvent-processed organic solar cells that are highly efficient and adaptable for the blade-coating method. Adv. Mater. *30*, https://doi.org/10.1002/adma.201704837.

Zheng, Z., Hu, Q., Zhang, S.Q., Zhang, D.Y., Wang, J.Q., Xie, S.K., Wang, R., Qin, Y.P., Li, W.N., Hong, L., et al. (2018). A highly efficient non-fullerene organic solar cell with a fill factor over 0.80 enabled by a fine-tuned hole-transporting layer. Adv. Mater. *30*, e1801801.

Zuo, L.J., Chueh, C.C., Xu, Y.X., Chen, K.S., Zang, Y., Li, C.Z., Chen, H., and Jen, A.K. (2014). Microcavity-enhanced light-trapping for highly efficient organic parallel tandem solar cells. Adv. Mater. *26*, 6778–6784.

ISCI, Volume *12*

Supplemental Information

Low-Energy-Loss Polymer Solar Cells with 14.52% Efficiency Enabled by Wide-Band-Gap Copolymers

Kui Feng, Jian Yuan, Zhaozhao Bi, Wei Ma, Xiaopeng Xu, Guangjun Zhang, and Qiang Peng

Transparent Methods

Materials and Characterization: ITIC and IT-4F were purchased from Derthon Optoelectronic Materials Science Technology. The organic tin monomer (M2 and M3) and naphtha[1,2-c:5,6-c]bis(1H-[1,2,3]triazole) (compound 1) were synthesized according to previous procedures (Dong et al. 2013; Zhang et al. 2018). All the other chemicals were purchased from Aladdin, Adamas, Sigma-Aldrich, and Alfa Asear Chemical Co., and used without further purification. All solvents were freshly distilled immediately prior to use.

Synthesis of Compound 2: Compound 1 (1.00 g, 4.78 mmol) was dissolved in the dimethyl sulfoxide (DMSO, 50 mL) at the room temperature. Sodium hydroxide (1.0 g, 25 mmol), tetrabutylammonium bromide (TBAB 0.1 g, 0.31 mmol) and 2-butyloctyl bromide (0.47 g, 0.19 mmol) were added successively under the protection of argon. The reaction was stirred under room temperature for 24 h. After that, the mixture was poured into ice water. The organic layer was extracted with dichloromethane and washed for several times with H_2O. The solution was dried over anhydrous $MgSO_4$ and concentrated by rotary evaporation. The residue was purified by column chromatography (SiO_2, petroleum ether:dichloromethane = 1:2) to give compound 2 as a colorless liquid (0.39 g, yield: 15.1%). ^{1}H NMR (400 MHz, $CDCl_3$, δ/ppm): 8.50-8.48 (d, 2H, *J* = 9.0 Hz, ArH), 8.00-7.99 (d, 2H, *J* = 9.0 Hz, ArH), 4.70-4.68 (d, 4H, *J*=7.1 Hz, N-CH_2), 2.39-2.38 (m, 2H, CH), 1.38-1.24 ((m, 32H, CH_2), 0.90-0.86 (t, 12H, CH_3). ^{13}C NMR (100 MHz, $CDCl_3$, *δ*/ppm): 142.9, 142.2, 122.6, 122.5, 117.3, 60.2, 39.2, 31.7, 31.4, 31.1, 29.7, 29.5, 28.4, 26.2, 22.9, 22.6,

14.1, 14.0. Anal. Calcd for $C_{34}H_{54}N_6$ (%): C 74.68, H 9.96, N 15.37; found (%): C 75.98, H 9.76, N 15.22.

Synthesis of Compound 3: After compound 2 (0.62 g, 1.15 mmol) was added in hydrobromic acid (20 mL), the temperature was raised until the solid was dissolved completely. Bromine (0.40 g, 2.53 mmol) was then added dropwise and the reaction was stirred overnight under reflux. After that, the excessive solution of sodium bisulfite was added to remove the excess bromine. The crude product was poured into 200 mL water and extracted by dichloromethane for three times. The solution was dried over anhydrous $MgSO_4$ and concentrated by rotary evaporation. The residue was purified by column chromatography (SiO_2, petroleum ether:dichloromethane = 1:1) to give compound 3 as a colorless liquid (0.54 g, yield: 68.2%). ^{1}H NMR (400 MHz, $CDCl_3$, δ/ppm): 8.64 (s, 2H, ArH), 4.72-4.71 (d, 4H, *J*=7.1 Hz, N-CH_2), 2.37-2.35 (m, 2H, CH), 1.38-1.25 ((m, 32H, CH_2), 0.89-0.86 (t, 12H, CH_3). ^{13}C NMR (100 MHz, $CDCl_3$, *δ*/ppm): 142.4, 141.1, 124.6, 122.3, 110.4, 60.7, 39.1, 31.7, 31.2, 31.0, 29.7, 29.5, 28.4, 26.1, 22.9, 14.1, 13.9. Anal. Calcd for $C_{34}H_{52}N_6Br_2$(%): C 57.95, H 7.44, N 11.93; found (%): C 75.98, H 7.76, N 15.53.

Synthesis of Compound 4: Compound 3 (0.5 g, 0.71 mmol), tributyl-(2-thienyl)-stannane (0.53 g, 1.42 mmol) and $Pd(PPh_3)_4$ (10 mg) were added in toluene. The mixture was stirred under the protection of argon and refluxed for 6 h. After the evaporation of the solvent, the product was purified by silica column chromatography (SiO_2, petroleum ether:dichloromethane = 1:1) to give compound 4 as an orange solid (0.41 g, yield: 81.2%). ^{1}H NMR(400 MHz, $CDCl_3$, δ/ppm): 8.69 (s,

2H, ArH), 8.27-8.26 (d, 2H, *J*=7.1 Hz, ArH), 7.45-7.43 (d, 2H, *J*=7.1 Hz, ArH), 7.24-7.23 (m, 2H, ArH), 4.77-4.76 (d, 4H, *J*=9.1 Hz, N-CH_2), 2.39-2.36 (m, 2H, CH), 1.38-1.29 (m, 32H, CH_2), 0.92-0.88 (t, 12H, CH_3). ^{13}C NMR (100 MHz, $CDCl_3$, *δ*/ppm): 140.1, 128.04, 127.7, 126.0, 123.9, 122.0, 118.0, 60.1, 39.2, 31.8, 31.4, 31.1, 29.6, 28.5, 26.2, 22.9, 22.67, 14.2, 14.0. Anal. Calcd for $C_{42}H_{58}N_6S_2$ (%): C 70.94, H 8.22, N 11.82; found (%): C 70.65, H 7.96, N 11.54.

Synthesis of Compound M1: Compound 4 (0.61 g, 0.857 mmol) was dissolved in THF (30 mL) and then N-bromosuccinimide (NBS) (0.33 g, 1.88 mmol) was added in several portions. The mixture was reacted for 8 h at the room temperature. After the evaporation of the solvent, the product was purified by silica column chromatography (SiO_2, petroleum ether:dichloromethane = 3:1) to give compound M1 as an orange solid (0.60 g, yield: 80.4%). ^{1}H NMR (400 MHz, $CDCl_3$, δ/ppm): 8.58 (s, 2H, ArH), 7.97-7.95 (d, 2H, *J*=3.9 Hz, ArH), 7.17-7.15 (d, 2H, *J*=3.9 Hz, ArH), 4.75-4.74 (d, 4H, *J*=6.8 Hz, N-CH_2), 2.39-2.36 (m, 2H, CH), 1.38-1.29 ((m, 32H, CH_2), 0.92-0.88 (t, 12H, CH_3). ^{13}C NMR (100 MHz, $CDCl_3$, *δ*/ppm): 141.4, 130.8, 127.0, 117.6, 113.7, 60.1, 39.2, 31.9, 31.7, 31.41, 31.1, 29.7, 29.5, 29.3, 28.4, 26.1, 22.9, 22.6, 14.0, 14.0, 1.03. Anal. Calcd for $C_{42}H_{56}N_6Br_2S_2$(%): C 58.06, H 6.50, N 9.67; found (%): C 58.35, H 6.46, N 9.87.

Synthesis of PBDTS-TZNT: M2 (0.350 g, 0.262 mmol) and M1 (0.227 g, 0.262 mmol) were first dissolved in 10 mL degassed toluene. After that, $Pd_2(dba)_3$ (4.7 mg, 2% mmol) and P(o-tol)$_3$ (6.3 mg, 8% mmol) were added into the above solution under argon atmosphere. The mixture was then stirred at 110 °C for 24 h in dark. After the

reaction mixture was cooled down to room temperature, it was dropped into 500 mL methanol. The resulting solid was collected by filtration, and then subjected to Soxhlet extraction successively with methanol, acetone, and hexane to remove the oligomers and impurities. The remaining polymer was dissolved in chloroform and precipitated again from methanol to yield PBDTS-TZNT as a dark solid (0.21 g, yield: 63.3%). ^{1}H NMR (400 MHz, $CDCl_3$, δ/ppm): 8.65-8.44 (br, 2H, ArH), 8.41-7.44 (br, 4H, ArH), 7.25-7.19 (br, 6H, ArH), 4.79-4.77 (br, 5H, N-CH_2), 3.12-3.10 (br, 4H, S-CH_2), 2.39-2.36 (m, 2H, CH), 1.52-1.19 (br, 64H, CH_2), 0.89-0.85 (br, 24H, CH_3). Anal. Calcd for $(C_{84}H_{112}N_6S_8)_n$ (%): C 68.99, H 7.72, N 5.75; found: C 68.89, H 7.51, N 5.61.

Synthesis of PBDTSF-TZNT: M3 (0.320 g, 0.233 mmol) and M1 (0.233 g, 0.233 mmol) were dissolved in 10 mL degassed toluene. After that, $Pd_2(dba)_3$ (4.2 mg, 2% mmol) and P(o-tol)$_3$ (5.7 mg, 8% mmol) were added into the above solution under argon atmosphere. The mixture was then stirred at 110 °C for 24 h in dark. After the reaction mixture was cooled down to room temperature, it was dropped into 500 mL methanol. The resulting solid was collected by filtration, and then subjected to Soxhlet extraction successively with methanol, acetone, and hexane to remove the oligomers and impurities. The remaining polymer was dissolved in chloroform and precipitated again from methanol to yield PBDTS-TZNT as a dark solid (0.20 g, yield: 60.1%). ^{1}H NMR (400 MHz, $CDCl_3$, δ/ppm): 8.65-8.40 (br, 2H, ArH), 8.39-7.40 (br, 2H, ArH), 7.25-7.19 (br, 6H, ArH), 4.82-4.80 (br, 5H, N-CH_2), 3.14-3.12 (br, 4H, S-CH_2), 2.50-2.42 (m, 2H, CH), 1.68-1.19 (br, 64H, CH_2),

0.89-0.85 (br, 24H, CH_3). Anal. Calcd for $(C_{84}H_{110}F_2N_6S_8)_n$ (%): C 67.33, H 7.40, N 5.61; found: C 67.54, H 7.32, N 5.85.

Instruments and characterization: ^1H and ^{13}C NMR spectra were recorded on a Bruker Avance-400 spectrometer with *d*-chloroform as solvent and chemical shifts were reported as δ value (ppm) relative to an internal tetramethylsilane (TMS) standard. The elemental analysis was performed on a Thermo Electron SPA Flash EA 1112 series analyzer. Molecular weights of the copolymers were determined by using a Waters 1515 GPC instrument with THF as the eluent and polystyrene as a standard. Thermogravimetric analysis was conducted on a TA Instrument Model SDT Q600 simultaneous TGA/DSC analyzer at a heating rate of 10 $^oC\ min^{-1}$ and under a N_2 flow rate of 90 mL min^{-1}. UV-vis spectra were obtained on a Cary 300 spectrophotometer. Cyclic voltammetry measurements were made on a CHI660 potentiostat/galvanostat electrochemical workstation at a scan rate of 50 mV s^{-1}, with a platinum wire counter electrode and an Ag/AgCl reference electrode in an anhydrous and nitrogen-saturated 0.1 mol L^{-1} acetonitrile solution of tetrabutylammonium perchlorate. The $CHCl_3$ solutions of the polymers were drop-coated onto the platinum plate working electrodes. 2D-GIWAXS measurements were performed at beamline 7.3.3 8 at the Advanced Light Source (ALS). R-SoXS transmission measurements were performed at beamline 11.0.1.2 at the ALS. AFM images were obtained by using a Bruker Inova atomic microscope in tapping mode. TEM images were obtained by using a ZEISS LIBRA 200 FE transmission electron microscope. SCLC is described by $J=9\varepsilon_0\varepsilon_r\mu V^2/8L^3$, where J is the current density, L is the film thickness of the active

layer, μ is the hole or electron mobility, ε_r is the relative dielectric constant of the transport medium, ε_0 is the permittivity of free space (8.85×10^{-12} F m^{-1}), *V* is the internal voltage in the device and $V = V_{appl}-V_{bi}-V_a$, where V_{appl} is the applied voltage to the device, V_{bi} is the built-in voltage due to the relative work function difference of the two electrodes and V_a is the voltage drop due to contact resistance and series resistance across the electrodes.

Single-junction device fabrication: The device structure was ITO/ZnO/copolymer:acceptor/MoO_3/Ag. The pre-patterned ITO glass substrates (sheet resistance = 15 Ω sq^{-1}) were ultrasonicated in detergent, deionized water, acetone, and isopropanol, subsequently. After dried by high-pressure air flow, the substrates were further cleaned by UV-ozone exposure for 30 min. A thin layer (30 nm) of ZnO was formed by spin-coating the precursor solution (diethylzinc solution 2M in toluene, diluted with THF) at 5000 rpm for 30 s, and then baked at 150 °C for about 20 min. The blend films of copolymer:acceptor (1:1, w/w) were prepared by spin-coating their solutions in CF:DIO (99.8:0.2, v/v) mixed solvent (total concentration: 14 mg mL^{-1}). The final film thickness was around 100 nm, detected by a Dektak 6 M surface profilometer. Thin layers of MoO_3 (10 nm) and Ag (100 nm) were then deposited on the top of surface in a high vacuum chamber (2×10^{-4} Pa). The device area was 4.0 mm^2.

Homo-tandem device fabrication: The homo-tandem device structure was ITO/ZnO/PBDTSF-TZNT:IT-4F/PEDOT:PSS/ultrathin Ag/ZnO/PBDTSF-TZNT: IT-4F/PEDOT:PSS/MoO_3/Ag. The fabrication of the bottom sub-cell was similar to

the single-junction device with the film thickness of 75 nm to guarantee sufficient light harvesting in the top sub-cell. Poly(3,4-ethylenedioxythiophene):polystyrene sulfonate (PEDOT:PSS) with 0.5 v% of Triton X-100 was spin-coated on the top of active layer of bottom cell (40 nm), followed by thermal evaporation of ultrathin Ag layer (5 nm) and ZnO nanoparticle layer spin-coating (30 nm), which formed the recombination layer. ZnO nanoparticles were synthesized by the previous literature (Beek et al. 2005). The active layer film thickness of the top cell varied from 85 to 125 nm to obtain a balanced current output in both sub-cells. Finally, thin layers of MoO_3 (10 nm) and Ag (100 nm) were deposited in a high vacuum chamber (2×10^{-4} Pa).

Device characterization: The I-V characterization of the devices was carried out on a computer-controlled Keithley 2400 Source Measurement system under 100 mW/cm^{-2} AM 1.5G light source, provided by a AAA solar simulator (XES-70S1, SAN-EI Electric Co., Ltd), which was calibrated with a standard Si solar cell (AK-200, KONICA MINOLTA, INC.). The EQE values were measured with a Newport QE test system (Newport Co., Ltd.) during illumination with monochromatic light from a xenon lamp, monitored by a traceable silicon photodiode.

Supplemental Figures

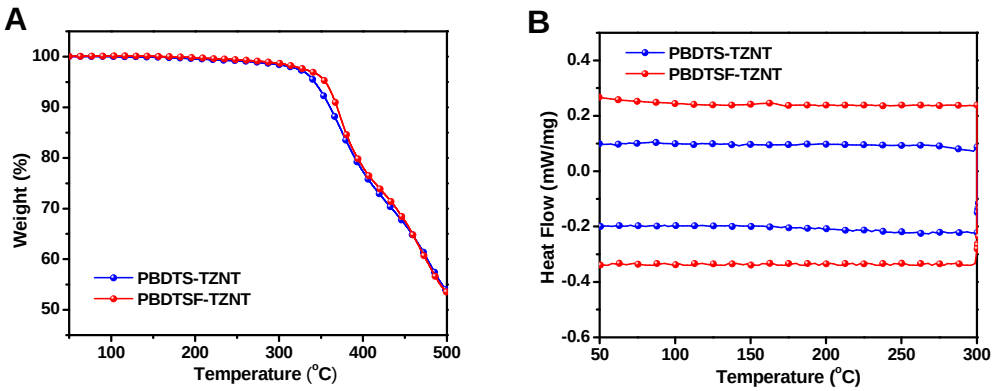

Figure S1. (**A**) TGA curves of the copolymers. (**B**) DSC curves of the copolymers. Related to Figure 1 and Scheme 1.

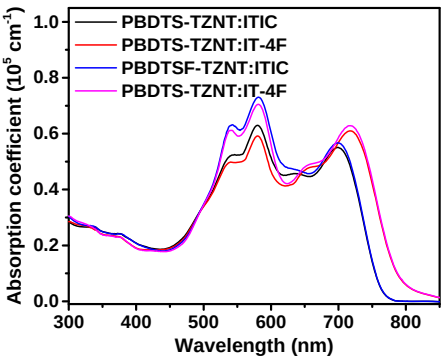

Figure S2. UV-vis spectra of the blend films. Related to Figure 2 and Table 1.

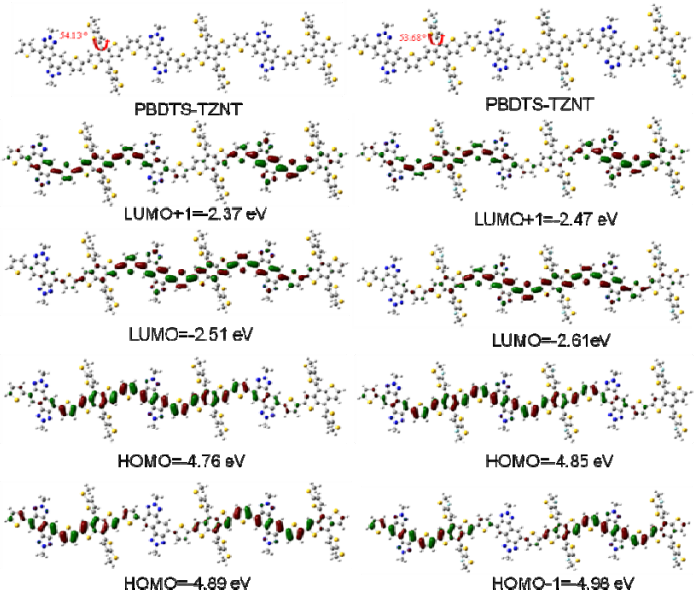

Figure S3. Optimized geometries of polymer trimers and the simulated energy levels**.** Related to Figure 2.

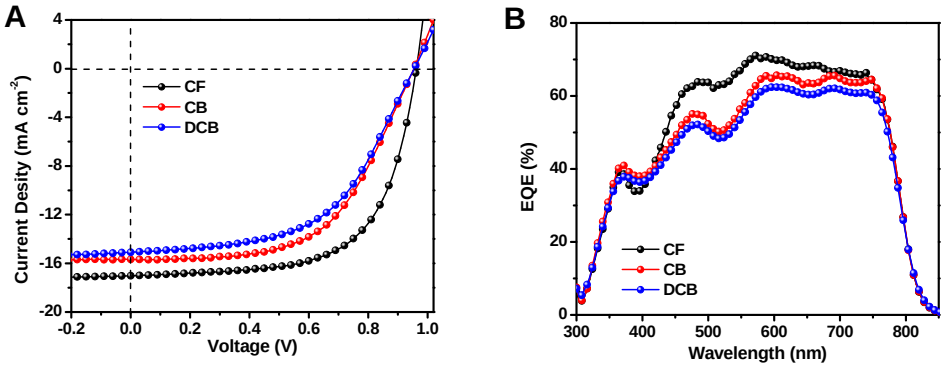

Figure S4. J-V curves (**A**) and EQE curves (**B**) of the PBDTSF-TZNT:IT-4F (1:1, w/w) devices processed from different solvents. Related to Figure 3 and Table 2.

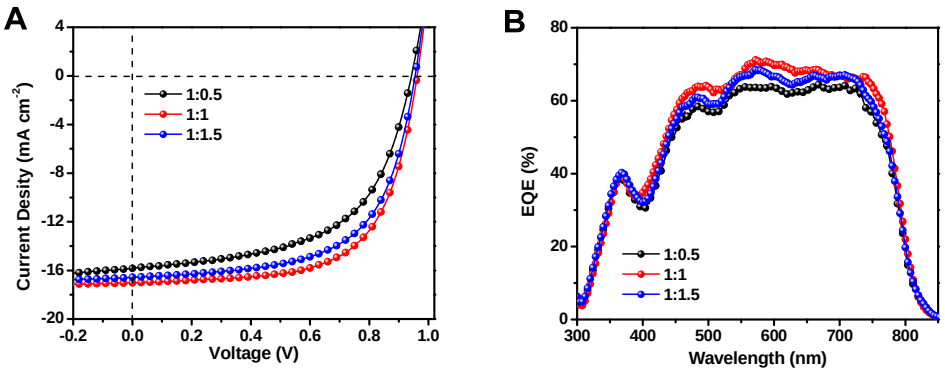

Figure S5. J-V curves (**A**) and EQE curves (**B**) of the PBDTSF-TZNT:IT-4F devices processed from CF with different D/A ratios. Related to Figure 3 and Table 2.

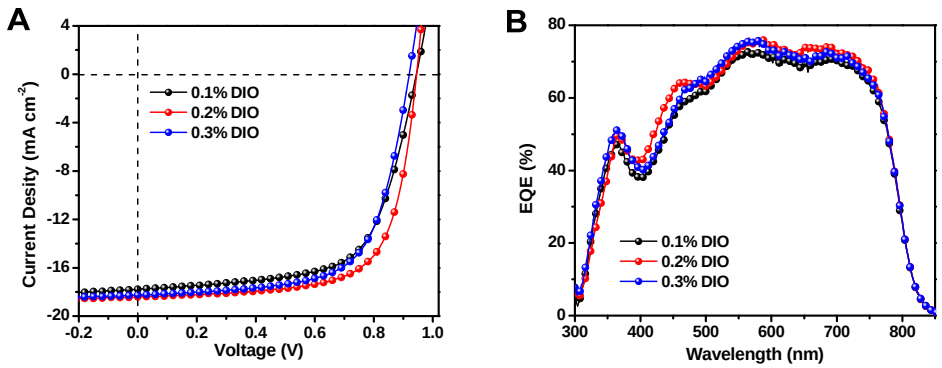

Figure S6. *J-V* curves (**A**) and EQE curves (**B**) of the PBDTSF-TZNT:IT-4F devices processed from CF with different additive content. Related to Figure 3 and Table 2.

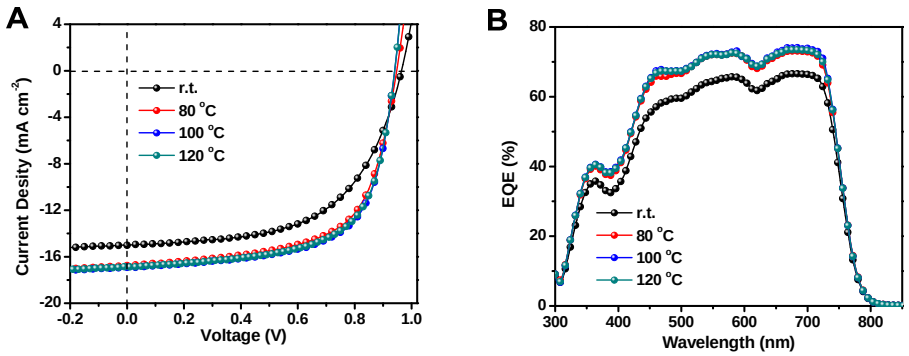

Figure S7. *J-V* curves (**A**) and EQE curves (**B**) of the PBDTS-TZNT:ITIC devices with different thermal annealing temperatures. Related to Figure 3 and Table 2.

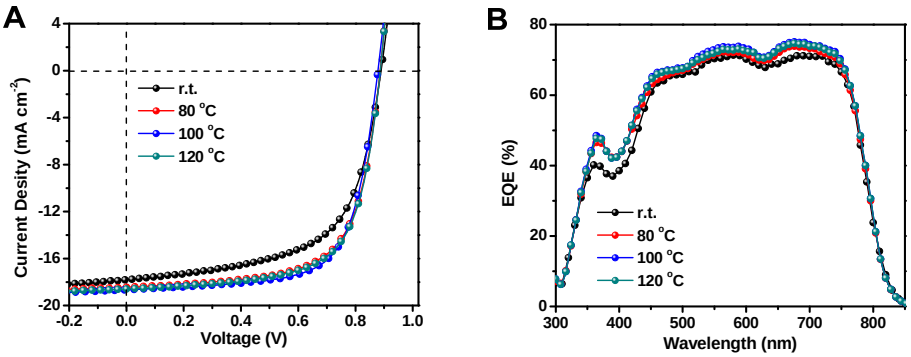

Figure S8. *J-V* curves (**A**) and EQE curves (**B**) of the PBDTS-TZNT:IT-4F devices with different thermal annealing temperatures. Related to Figure 3 and Table 2.

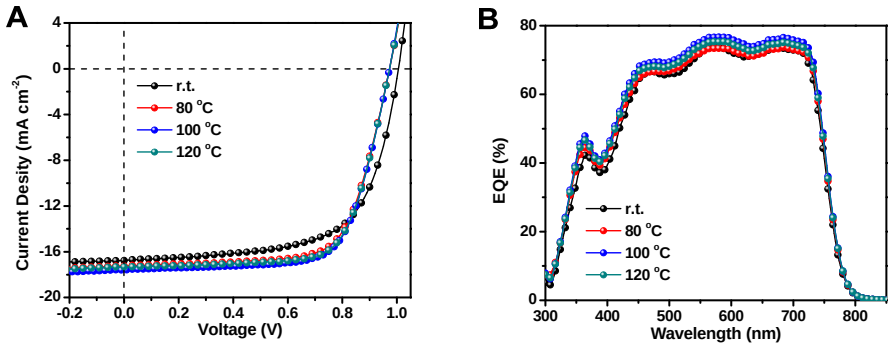

Figure S9. *J-V* curves (**A**) and EQE curves (**B**) of the PBDTSF-TZNT:ITIC devices with different thermal annealing temperatures. Related to Figure 3 and Table 2.

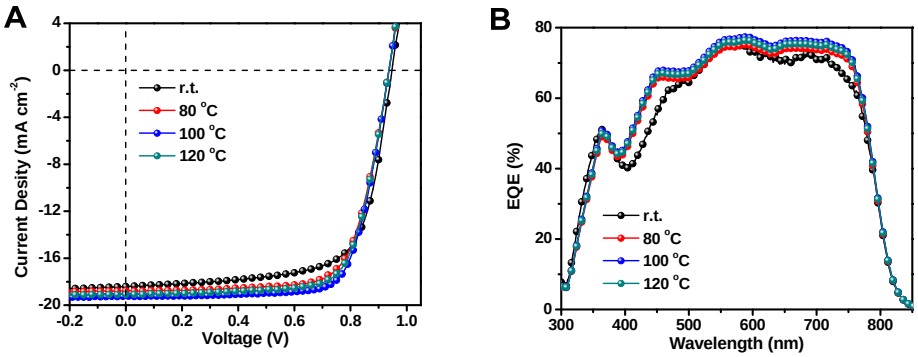

Figure S10. *J-V* curves (**A**) and EQE curves (**B**) of the PBDTSF-TZNT:IT-4F devices with different thermal annealing temperatures. Related to Figure 3 and Table 2.

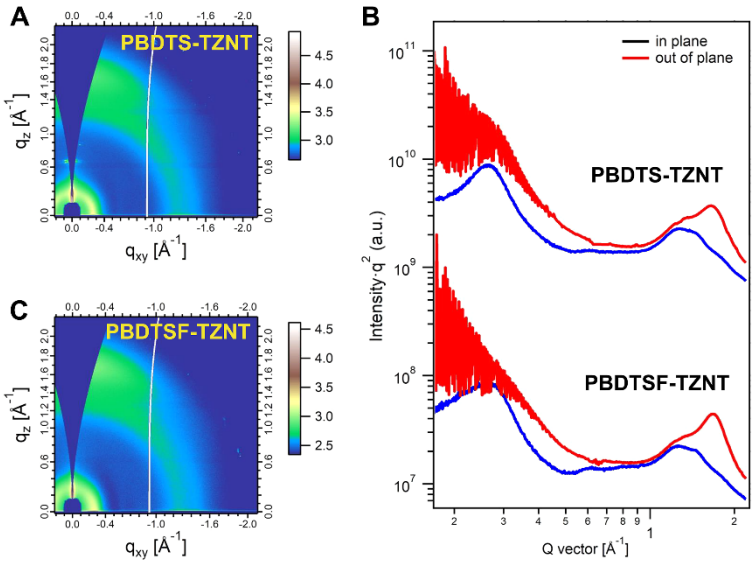

Figure S11. (**A,B**) GIWAXS patterns of pristine polymer films. (**C**) In-plane and out-of-plane line-cut profiles. Related to Figure 4.

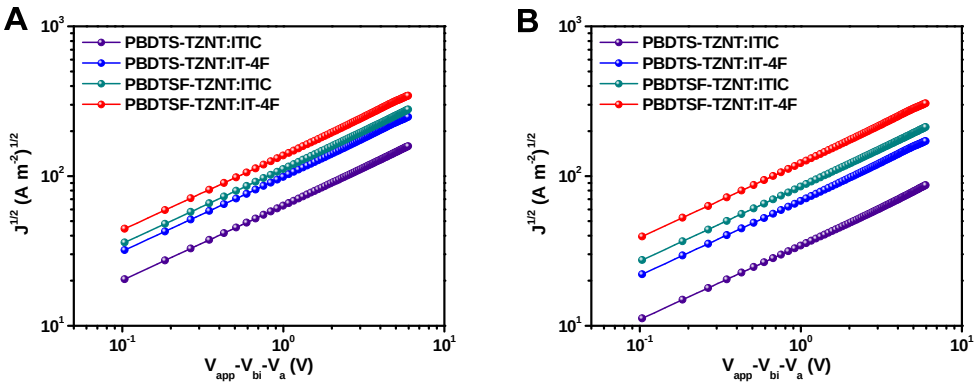

Figure S12. $J^{1/2}$-V curves of the hole-only (**A**) and electron-only (**B**) devices. Related to Figure 4.

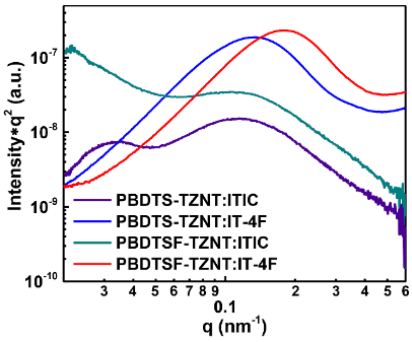

Figure S13. R-SoXS profiles of the blend films. Related to Figure 5.

160017113185 (2016)国认监认字(446)号

中国认可 国际互认 检测 TESTING CNAS L6673

Test Report

Test Report No. AGXB118W00655

Product name	Homo-Tandem Solar Cell
Manufacturing unit	Sichuan University
Commission unit	Sichuan University
Inspection category	Commissioned inspection

National Photovoltaic Product Quality Supervision & Inspection Center

National Photovoltaic Product Quality Supervision & Inspection Center
TEST REPORT

Test Report No. AGXB118W00655

Product name	Homo-Tandem Solar Cell	Trade Mark	/
Date of manufacture	11/26/2018	Model / type	/
Sample No.	1#	Sample grade	Qualified product
Sample quantity	one piece	Sample state	/
Date of arrival	11/26/2018	Sample delivery personnel	Qiang Peng
Commission unit	Sichuan University	Manufacturing unit	Sichuan University
Commission unit address	No.29 Wangjiang Road, Chengdu, Sichuan, P. R. China.	Manufacturing unit address	No.29 Wangjiang Road, Chengdu, Sichuan, P. R. China.
Commission unit Zip code	610064	Manufacturing unit Zip code	610064
Commission unit Tel.	15828019886	Manufacturing unit Tel.	15828019886
Test Address	No 355, 2nd Tengfei Road, Southwest Airport Economic Development Zone, Chengdu, Sichuan, P. R. China.	Testing Period	11/27/2018
Test Standard	IEC60904-1:2006 Photovoltaic devices -Part 1: Measurement of Photovoltaic Current-Voltage Characteristics.		
Test conclusion	This column blank		(Special chapter for test report)
Remarks	/		

Date: 11/28/2018

Approved by 12月

Witnessed by 白晓东

Tested by

National Photovoltaic Product Quality
Supervision & Inspection Center
TEST REPORT

Test Report No. AGXB118W00655 Page 2 of 2

Test Results:

Clause	Test item(s)	Unit	Results
1	Current-voltage characteristics measurement	---	---
1.1	Open-circuit voltage, Voc	V	1.800
1.2	Short-circuit current, Isc	mA	0.451
1.3	Short-circuit current density, Jsc	mA/cm^2	11.287
1.4	Maximum-power, Pmax	mW	0.566
1.5	Maximum-power voltage, Vpmax	V	1.440
1.6	Maximum-power current, Ipmax	mA	0.393
1.7	Fill factor, FF	%	69.61
1.8	Conversion efficiency, η	%	14.14

Current Voltage characteristic at STC

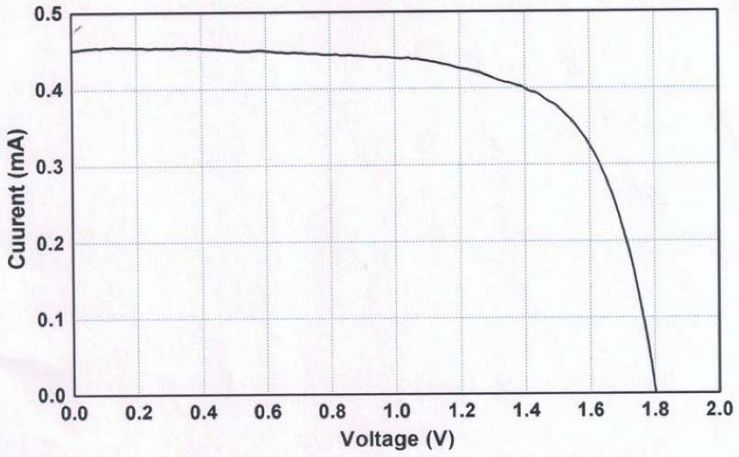

Remark: Sample was tested with a mask under the irradiation with a steady-state class calibrated AAA solar simulator. Working sample area (S) is determined by aperture outer range on the mask, S=4.00 mm^2.

----Blank----

Figure S14. Certification of the homo-tandem device based on PBDTSF-TZNT:IT-4F in National Photovoltaic Product Quality Supervision & Inspection Center of China. Related to Figure 6.

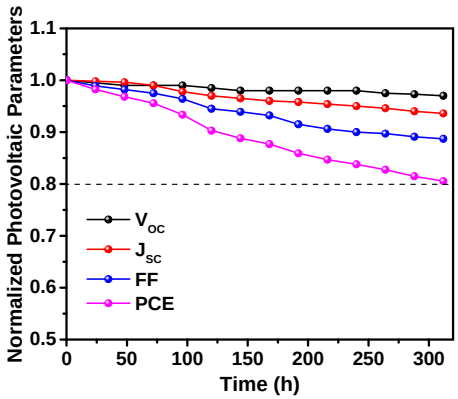

Figure S15. Normalized PCEs of the homo-tandem device based on PBDTSF-TZNT:IT-4F kept in glove box. Related to Figure 6.

Supplemental Tables

Table S1. Photovoltaic parameters of the PBDTSF-TZNT:IT-4F (1:1, w/w) devices processed from different solvents. Related to Figure 3 and Table 2.

solvent	Concentration (mg/mL)	V_{oc} (V)	J_{sc} (mA/cm^2)	J_{EQE} (mA cm^{-2})	FF (%)	PCE (%)
CF	14	0.96	17.02	16.79	64.1	10.48
CB	20	0.95	15.68	15.51	56.3	8.39
DCB	25	0.95	15.10	14.78	54.4	7.80

Table S2. Photovoltaic parameters of the PBDTSF-TZNT:IT-4F processed from CF with different D/A ratios and additive content. Related to Figure 3 and Table 2.

D/A	DIO (v%)	V_{oc} (V)	J_{sc} (mA/cm^2)	J_{EQE} (mA cm^{-2})	FF (%)	PCE (%)
1:0.5	-	0.94	15.83	15.44	57.1	8.50
1:1	-	0.96	17.02	16.79	64.1	10.48
1:1.5	-	0.95	16.57	16.16	62.2	9.79
1:1	0.1	0.94	17.78	17.25	65.6	10.97
1:1	0.2	0.94	18.41	18.10	70.1	12.13
1:1	0.3	0.93	18.25	17.83	66.8	11.34

Table S3. Photovoltaic parameters of the NF-PSCs treated with different thermal annealing temperatures. Related to Figure 3 and Table 2.

Active layer	Temp. (^{o}C)	V_{oc} (V)	J_{sc} (mA/cm^2)	J_{EQE} (mA cm^{-2})	FF (%)	PCE (%)
	r.t.	0.96	15.01	14.63	58.3	8.40
PBDTS-TZNT:ITIC	80	0.94	16.76	16.29	64.2	10.12
(1:1, CF, 0.2v%DIO)	100	0.94	16.92	16.45	65.7	10.45
	120	0.94	16.87	16.36	65.1	10.33
PBDTS-TZNT:IT-4F	r.t.	0.89	17.78	17.22	61.8	9.78
(1:1, CF, 0.2v%DIO)	80	0.88	18.43	18.01	67.1	10.89

	100	0.88	18.65	18.23	68.9	11.31
	120	0.88	18.58	18.12	67.9	11.10
	r.t.	1.00	16.76	16.31	65.5	10.98
PBDTSF-TZNT:ITIC	80	0.98	17.24	16.54	69.1	11.67
(1:1, CF, 0.2v%DIO)	100	0.98	17.58	17.22	70.6	12.16
	120	0.98	17.32	16.91	70.3	11.93
	r.t.	0.94	18.41	18.10	70.1	12.13
PBDTSF-TZNT:IT-4F	80	0.93	18.78	18.49	72.6	12.68
(1:1, CF, 0.2v%DIO)	100	0.93	19.23	18.97	74.1	13.25
	120	0.93	19.07	18.81	73.2	12.99

Table S4. Summarized parameters for the ordered molecular structures. Related to Figure 4.

Blend film	lamellar stacking	π-π stacking		
	d_l [Å] (q_{xy} [$Å^{-1}$])	d_π [Å] (q_z [$Å^{-1}$])	FWHM [$Å^{-1}$][a]	L_C [Å][b]
PBDTS-TZNT	25.1 (0.25)	3.61 (1.73)	0.27	23
PBDTSF-TZNT	25.1 (0.25)	3.59 (1.74)	0.25	25
PBDTS-TZNT:ITIC	25.1 (0.25)	3.65 (1.72)	0.39	16
PBDTS-TZNT:IT-4F	25.1 (0.25)	3.63 (1.73)	0.24	26
PBDTSF-TZNT:ITIC	25.1 (0.25)	3.63 (1.73)	0.28	22
PBDTSF-TZNT:IT-4F	25.1 (0.25)	3.61 (1.74)	0.21	30

[a]Full width at half-maximum (FWHM) for the (010) peak along the q_z axis.

[b]Coherent length estimated from the Scherrer's equation ($L_C = 2\pi/FWHM$) for the π-π stacking of the face-on crystallite.

Supplemental References

Beek, W.J., Wienk, M.M., Kemerink, M., Yang, X., and Janssen, R.A. (2005). Hybrid zinc oxide conjugated polymer bulk heterojunction solar cells. J. Phys. Chem. B *109*, 9505-9516.

Dong, Y., Hu, X.W., Duan, C.H., Liu, P., Liu, S.J., Lan, L.Y., Chen, D.C., Ying, L., Su, S.J., Gong, X., Huang, F., and Cao, Y. (2013). A series of new medium-bandgap conjugated polymers based on naphtho[1,2-c:5,6-c]bis(2-octyl-[1,2,3]triazole) for high-performance polymer solar cells. Adv. Mater. *25*, 3683-3688.

Zhang, G.J., Xu, X.P., Bi, Z.Z., Ma, W., Tang, D.S., Li, Y., and Peng, Q. (2018). Fluorinated and alkylthiolated polymeric donors enable both efficient fullerene and nonfullerene polymer solar cells. Adv. Funct. Mater. *28*, 1706404.